

**3D VISION MEASUREMENT SYSTEM
FOR
INTELLIGENT OPEN-DIE FORGING CENTER**

**3D VISION MEASUREMENT SYSTEM
FOR
INTELLIGENT OPEN-DIE FORGING CENTER**

By
BING LI, B. Eng

A Thesis

Submitted to the School of Graduate Studies
in Partial Fulfillment of the Requirements
for the Degree
Master of Applied Science

McMaster University

© Copyright by Bing Li, September 2007

MASTER OF APPLIED SCIENCE (2007)

McMaster University

Mechanical Engineering

Hamilton, Ontario

TITLE: 3D Vision Measurement System for Intelligent Open-Die
Center

AUTHOR: Bing Li, B. Eng
(University of Shanghai for Science & Technology, China)

SUPERVISOR: Dr. Tim Nye, Associate Professor.

NUMBER OF PAGES: x, 113

To My Parents Changhe and Fenghua

Abstract

In this thesis, a 3-D vision system is established to conduct the real-time measurement task for intelligent open-die forging center. This system consists of a CCD camera, a slit laser projector and a Kawasaki JS 6-axis robot all interfaced to a PC for image processing.

The linear structured light technique is employed for data acquisition. An optical filtering algorithm for laser stripe segmentation is developed to locate the stripe peak positions to sub-pixel accuracy. A new calibration method is proposed to determine the mapping correspondence from 2-D image pixels to 3-D reference points. A cylindrical scanning scheme is applied to gather data about the 3-D shape of parts, so that the overlap problem is easily avoided. Finally, the cross-section at any place along the height of a workpiece is reconstructed so as to detect shape error for adaptive control of automated open-die forging.

This vision system is low-cost, accurate and reliable. A cylinder shape has been successfully reconstructed and measured with it. The experimental results illustrating its performance are reported and discussed.

Acknowledgements

I would like to express my greatest gratitude to my supervisor Dr Tim Nye for his invaluable guidance and moral support in all the time of research for and writing of this thesis. I also sincerely thank all the professors, colleagues and staff at Mechanical Engineering Department, specially our research technician Mr. Mark MacKenzie for all his assistance on the experiments with the robot.

Especially, I am deeply indebted to my dear wife Zhaolu whose patient cares to our daughter enabled me to concentrate on and complete this work.

Contents

Abstract	ii
Acknowledgements	iii
List of Tables	vii
List of Figures	viii
1 Introduction	1
1.1 Background and Motivation	1
1.2 Overview of the Approaches	5
1.3 Scope of Work	7
2 Literature Review	8
2.1 Introduction.....	8
2.2 Techniques of 3D Shape Measurement	9
2.2.1 Passive Techniques	9
2.2.2 Active Techniques	10
2.3 The Slit Laser Scanner.....	11
2.3.1 Laser Stripe Detection.....	13
2.3.2 Calibration.....	14
2.4 View Registration	19
2.5 Shape Reconstruction.....	20
2.6 Summary	20

3	Methodology and System Design	21
3.1	System Setup.....	22
3.1.1	Arrangement of a Camera and a Laser Projector in a Rigid Frame.....	22
3.1.2	Hardware Description	27
3.1.3	Kawasaki Six-Axis Robot Control.....	28
3.2	Laser Stripe Segmentation	31
3.2.1	Adjustment of Camera Physical Parameters.....	32
3.2.2	Background Subtraction.....	32
3.2.2	Sub-pixel Peak Estimation Algorithm	41
3.3	Calibration.....	46
3.3.1	Basic Concept	46
3.3.2	Calibration Process Description.....	50
3.3.3	Determining Image-to-Model Homography	54
3.3.4	3D Reference Coordinates of Laser Stripe Points in Model Plane.....	57
3.3.5	Fitting the Laser Projection Plane.....	58
3.3.6	A Model of Laser Projection.....	60
3.3.7	Determining the Matrix from the Projection Plane to the Reference System.....	61
3.3.8	Image-to-Projection Homography Matrix	63
3.3.9	Image-to-Reference Transformation Matrix.....	64
3.3.10	Results and Analysis	65
3.4	360-Degrees Measurement	70
3.4.1	Scanning Schemes	70
3.4.2	Cylindrical Scanning.....	72
3.4.3	Determination of the Revolution Axis of the Manipulator in the Reference system	76
3.4.4	Point Cloud	80
3.4.5	Range Image	82

3.4.6	Noise Elimination	84
3.5	Geometry Measurement in Intelligent Open Die Forging System	91
3.5.1	Function of the 3-D Vision System in Intelligent Forging System	91
3.5.2	Shape Error Detection.....	92
3.5.3	Application in the Cylindrical Scanning Vision System	94
3.5.4	Reconstruction Algorithm of a Cross-Section of Workpiece at a Height	96
3.6	The 3-D Measurement Software	99
4	Experimental Results and Analysis	100
4.1	Experimental Results	100
4.2	Analysis.....	104
5	Conclusions and Recommendations	108
5.1	Conclusions.....	108
5.2	Recommendations for Future Work.....	110
	REFERENCES	111

List of Tables

3.1	The experimental errors when using computed homography matrix	57
3.2	Reconstruction errors relative to the calibration points	67
3.3	Determination of Z-coordinate of calibration points	68
3.4	The threshold values for local smooth test	87

List of figures

1.1	losed control loop of automatic open die forging	3
1.2	A sketch of the 3-D vision system	5
2.1	Binocular stereovision	10
2.2	A typical slit scanner configuration	12
2.3	A projective model of a structured light	15
2.4	The principle of the direct calibration method by Wang	17
2.5	Huynh’s calibration method.....	18
3.1	A 3D triangulation of a linear structured light system.....	23
3.2	Trade -off between the length and the view of a camera	25
3.3	The rigid frame of a CCD camera and a laser projector	26
3.4	Hardware connections of the vision system.....	27
3.5	Communication between the robot controller and the computer.....	29
3.6	The flow chart of function send_receive().....	30
3.7	Procedure for subtracting background	33
3.8	RGB Color Cube for uint8 Images	34
3.9	A picture of the captured scene.....	38
3.10	The normalized RGB image	39
3.11	The red color tracking image.	39
3.12	A region of interest detected by RGB thresholds	39

3.13	The filtered image	40
3.14	A segmented laser stripe	40
3.15	Observed peak of stripe	40
3.16	Histogram of one row intensities	42
3.17	A fitted intensity function curve	43
3.18	The result of Center of Mass.....	45
3.19	The result of the Gaussian estimator.....	45
3.20	A pinhole camera model	47
3.21	Plane to plane homography.....	49
3.22	Calibration process description.....	53
3.23	Extracted corners in the model plane.....	54
3.24	Algorithm of the determination of corner coordinates in model plane.....	55
3.25	Comparison of actual and computed corners.....	56
3.26	The detected calibration points in the laser plane	58
3.27	A laser projection model	60
3.28	The detected laser points (in red) reconstructed by equation 3.44	66
3.29	The results of depth comparison	68
3.30	A length measured with the proposed calibration method.....	69
3.31	Linear and cylindrical scanning process	70
3.32	Position of the revolution axis in the reference system	73
3.33	The program of cylindrical scanning vision measurement	75
3.34	A fixture to position revolution axis	77
3.35	A laser line projected on the fixture at different angls.....	79

3.36	Cylindrical scan Images of a workpiece	80
3.37	Noisy point cloud.....	81
3.38	A data structure to store the laser points in sub-pixel accuracy.....	83
3.39	An example of range image	83
3.40	Multi-peaks problem.....	85
3.41	Inter-reflection phenomenon.....	85
3.42	A bar illuminated by the laser	86
3.43	Noise points detected through filtering.....	88
3.44	The resultant point cloud after local smoothness test	88
3.45	The result of median filter.....	90
3.46	An intelligent open-die forging system (revised from Li’s system)	91
3.47	The process of forging a workpiece by a robot.....	93
3.48	A cylindrical scanning model	94
3.49	Flow chart of the cross-section reconstruction	96
3.50	The flow chart of 3-D measurement software	99
4.1	3-D shape by cross-section representation.....	102
4.2	Reconstruction of a cylinder by cross-section representation.....	103
4.3	The errors of circle fitting and reconstruction diameter along the height.....	104
4.4	A fitted circle at height=68mm	104
4.5	A fitted circle at height=5mm	105
4.6	A fitted circle at height=1 mm	106
4.7	A fitted circle at height=69mm	105
4.8	A forged part reconstructed by 3-D vision system	108

Chapter 1

Introduction

1.1 Background and Motivation

Forging is a metalworking process where workpiece is controllably, plastically deformed into predetermined shapes by means of compressive forces or impact blows, or a combination of both (Jenson, 1966). Through forging, quality of the metal is improved, with refined grain structure, increased strength and toughness.

Forging can be implemented under hot or cold-working conditions. Hot forging occurs when the metal is deformed plastically above its recrystallization temperature. In this case, material is highly ductile, thus strain hardening can be avoided. Cold forging is generally limited to relatively soft materials, in which metal is not heated. The primary advantage of the forging process is material savings achieved through precision shapes that require little finishing.

Forging can be carried out in closed-dies or open-dies. In closed-die forging, material is confined in a closed die and flows severely to deform into a determined geometry. Good tolerances and accuracy of final shape can be attained. But due to high property requirements and machining costs, the dies used in this process are fairly expensive. Open-die forging is known as hand, smith, hammer, and flat-die forging. The process

manipulates a workpiece and shapes it under a sequence of hammering actions. Usually, open-die forging consists of a pair of flat dies – one attached to the hammer or to the press ram; and the other attached to the anvil. The swaging dies, V-dies, the combination of V-dies and flat dies, pins and loose tools are also used to produce specific shapes.

Open-die forging is an incremental process. At each pass, only one part of material is deformed. The resultant load used to produce a given part is relatively lower. But its accomplishment embraces a tremendous amount of operator skill and empirical knowledge. Automation of this incremental process would meet the need of more flexibility of forging and savings in labor.

The main idea is compressing and upsetting material bite by bite, at the same time, the position of the workpiece is automatically changed by the manipulator so as to decrease shape errors, until it reaches the target shape (Aksaka et al. 1997). Motions of the manipulator and the press are integrated into a control program. In order to achieve the desirable shape, a programmed schedule needs to be made for each incremental bite. The control system should have the ability to know where the hammer or press deforms the metal part and how much force should be applied like what a skilled blacksmith does. But in practice, the realization of this system is hard to be made.

During the open die forging process, material flows freely without severe constraints. In order to maintain a constant volume, material elongates and spreads sideways. Because the ends of workpiece are rigid and the friction on the contact area between tools and workpiece prevents exterior material of workpiece from flowing freely, the sideways spread of material is not uniform. Thus, when the thickness is reduced to the final size we

need, a bulge appears. Compressing workpiece after 90 degree of rotation, the same phenomenon happens again. Therefore, the movements of press and manipulator must accommodate the uneven spread and elongation which complicate the program to control the forging system.

Most researchers have tried to obtain an analytic model to predict this phenomenon of material flow. Tomlinson and Stringer (1959) first introduced the spread coefficient “ s ” defined as the ratio of the elongation to side-way spread, and developed an empirical equation for predicting the deformation behavior. With this specific coefficient, a theory of forging schedules is derived (Wistreich and Shutt, 1959), in that the increase of both the length and width of forged parts, which are caused by the compression during each forging squeeze, can be predicted in advance. After their pioneering work, many models used to estimate the spread coefficient have been induced either from analysis or experiences. However, these models are not in good agreement with the experimental results, especially when the process parameters are changed.

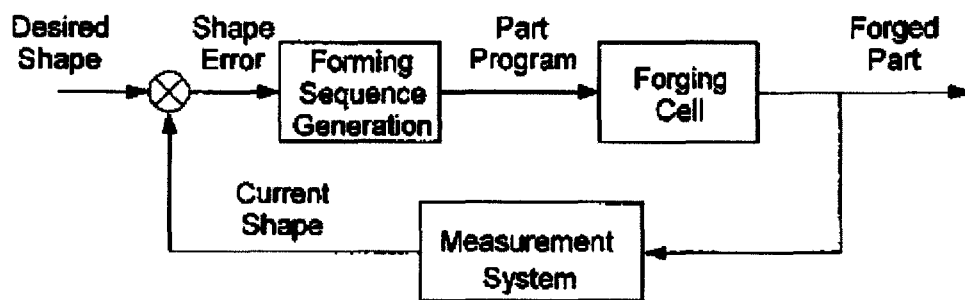


Figure 1.1: Closed control loop of automatic open die forging (Nye, 2001).

In 2001, Nye et al proposed an adaptive control program to automate open die forging. The concept of this control program is shown in Fig 1.1. In such system, the shape error of forged part between current shape and target shape is measured in real time and input into a control closed loop as a feedback, with which the forging schedule can be frequently regenerated in light of actual process conditions until the target shape is approximately achieved. The experimental results proved this feasibility. But the measurement method they applied mainly depends on a manipulator compliance system. Due to the fact the robot vibrations always exist, the elongation data obtained from the manipulator displacement might not be accurate enough to detect the shape error.

Based on Nye's research, an intelligent open die forging system was integrated by Li Ma (2004). The forging cell mainly consists of a hydraulic press, a 6-axis robot and 2-D vision system. While forging, the robot holds the workpiece to be processed in the press. After each step of forging, the robot will move the workpiece to the camera for vision measurement. According to the cross-section shape error, a forging sequence is generated by the control unit. The robot is then commanded to implement appropriate manipulation of workpiece for forging.

Ma's forging system works well to forge a part from square to round shapes. But for the parts with complex shapes like concave and convex shapes, since only one cross-section can be detected by the 2-D vision system, failures in forging them will be expected. Therefore, further research needs to be made on the development of 3-D measurement system so that the working capability of the intelligent forging system can be improved.

1.2 Overview of the Approaches

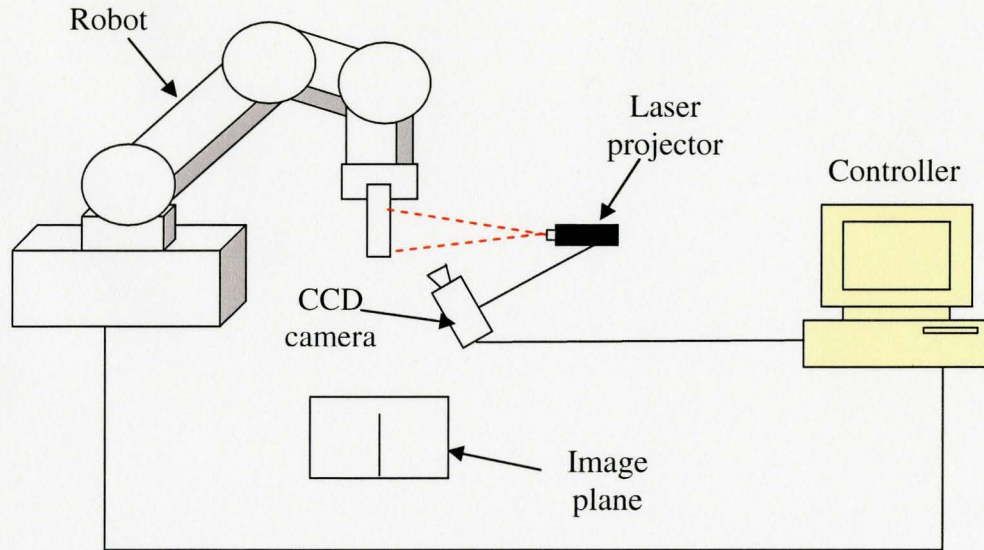


Figure 1.2: A sketch of the 3-D vision system.

In this thesis, a 3D vision system is established to implement the 3D measurement task in real-time. The system applies the linear structured light to acquire the geometric shape of object. A sketch of such system is shown in Fig.1.2. It simply consists of a laser slit projector and a CCD camera, both of which are installed on a rigid frame fixed on the working table. A Kawasaki 6-axes robot is controlled to perform linear movement and rotation for providing the whole views of object.

The basic principle of this vision system is to scan a workpiece with a laser beam and then to detect the location of the reflected line. While scanning, a sequence of scan images is taken by the camera. Through image processing in each image, the laser stripe created by intersection of the projection plane with the workpiece surface is segmented. A Gaussian approximation algorithm is then employed to estimate the stripe peak image

positions to sub-pixel accuracy.

A fast calibration method is proposed to determine the transformation relationship from 2-D image plane to 3-D reference coordinates system. It is easily carried out by the manipulator holding and shifting a planar chessboard to a series of positions in the reference system, during which the laser beam is always projected onto the chessboard surface and the illuminated scene is captured by the camera. Inspired by Zhang's technique (Zhang, 1999), a homography matrix between the chessboard plane and the image plane can be computed at any shifting position. Thus, by using this specific matrix and a corresponding position, any laser pixel detected on the chessboard can be transformed into a 3-D point with respect to the reference coordinates system. In this way, a number of 3-D calibration points are obtained and then used to fit the projection plane with the least squares method. With this resultant plane, Huynh's projective model is applied to determine the optical triangulation of laser projection with camera and define it by an image-to-world transformation matrix (Huynh et al, 1999).

A cylindrical scanning scheme is adopted for gathering 3D point data from the entire surface. The scanning movement is to rotate 360 degree around the revolution axis of the 6th joint of the robot. A special fixture is designed to locate the axis position in the reference system, so that 360-degree scans of a workpiece can be integrated into a common coordinates system with the robot transformation matrix. As a result, a digitized point cloud is achieved for the whole workpiece profile. After filtering the noisy point data by means of local smoothness test and mean filter, a shape reconstruction algorithm is finally programmed to measure a cross-section of the workpiece at any place along the

length.

All algorithms for 3D vision measurement and control programs in this thesis are written by C++ and OpenCv library (Intel, 2006), and the reconstructed shapes of measured parts are visualized with Matlab.

1.3 Scope of Work

In this thesis, a 3D vision measurement system is designed for the intelligent open-die forging center. It adapts to the context of forging conditions and provides the ways to acquire 3-D geometric shape of a forged part. An aluminum bar consisting a cylinder shape is used as the test workpiece in experiments. Its cross-section at any height is successfully reconstructed and each measured surface point is defined by a cylindrical coordinate, which will be applied for shape error detection.

Chapter 2 gives a review of related works in 3D vision measurement and summarizes what has been done and what will be adopted for building up a vision system. In chapter 3, design methodology is given in detail. The programs of laser stripe segmentation and peak estimation to sub-pixel accuracy are explained first. The algorithms for calibration, cylindrical scanning scheme and cross-section reconstruction are introduced afterward. Chapter 4 presents the experimental results over this system and accuracy analysis by comparing the reconstructed cylinder with the actual one measured with a digital caliper. The conclusions of the research are provided in chapter 5.

Chapter 2

Literature Review

2.1 Introduction

Dimensional measurement of a forged part is essentially for real-time process control in open die forging. Traditionally, manual, contact measurement is applied with some simple tools. For example, Nye et al. (2001) used dial gauges to measure the height of the workpiece and the position of the center of the compliance device. Limited work has been done on automatic measurements. In the system reported by Siemer et al (1986), data acquisition is by way of detecting the back-forth position of a spring-loaded cable attached to the end of the forging. Due to the potential problem that the cable may interfere with other process equipments, this approach is only practical in laboratory experiments but not in practice. In 2001, Nye et al designed a passive compliance end effector to accommodate the deformation of workpiece during press. A linear potentiometer was utilized to measure the displacement of the end-effector in the elongation direction. However, two restrictions encumber the application of this method, which are robot vibration and 1-dimensional measurement.

Ma employed machine vision technology to conduct no-contact gauging on an aluminum bar (Ma, 2004). As the bar rotates 360 degree, a sequence of pictures is taken

by a CCD camera. Through image processing by means of noise filtering and Sobel edge detection, a cross-section silhouette of the forged bar is extracted. Her method was shown to be useful for determining a single simple shape of workpiece such as square or round but was not able to detect overall dimensions of the workpiece for complicated shapes with convex and concave features.

Taking advantage of rapid developments of 3-D vision techniques, 3-D surface of the object can be fully recovered. But for the particular application in open die forging, there are still some technical issues that need to be studied such as data acquisition, image processing and surface reconstruction. The next contents of this chapter will review different kinds of 3-D vision techniques and compare them to explore the ways of implementing 3-D measurement of forged parts.

2.2 Techniques of 3D Shape Measurement

Most techniques for 3-D shape measurement are summarized in a review made by Frank et al (2000). Generally, based on whether an extra energy source besides the natural ones like the ambient lighting is used or not, they can be classified into active and passive techniques.

2.2.1 Passive Techniques

In contrast to active techniques that use an external projecting device, the class of techniques to extract 3-D information with visual cues(e.g. stereoscopic disparity, texture, motion parallax, (de)focus, shadows, shading and specularities, occluding contours and other surface discontinuities) contained in images, is called passive (Ali et al., 2003) .

One of the well-known passive methods is stereo vision. As shown in Fig. 2.1, it uses two or more cameras to obtain stereoscopic disparity with which the depth of object is determined (Garcia et al, 2001). There are obvious advantages of this method: cost, simplicity of imaging hardware, and compatibility with human visual processes. But the major difficulty is finding the correspondence between two images. For example, in Fig. 2.1, two cameras C_1 and C_2 capture 2D images of a scene. In these images points $P_1(u_1, v_1)$ and $P_2(u_2, v_2)$ correspond to point $P(X, Y, Z)$ in the scene. The correspondence problem is to identify that P_1 and P_2 in each camera image represent point P in the scene. In forging, the part surface has very few unique features that can be used to determine this correspondence between images.

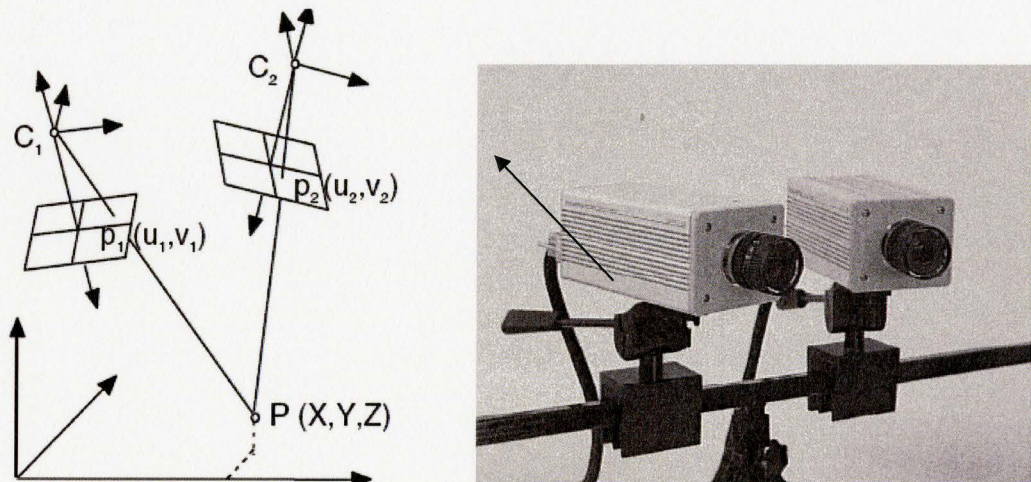


Figure 2.1: Binocular stereovision (Garcia et al, 2001).

2.2.2 Active Techniques

The active techniques can produce more dense and accurate 3-D data than the

passive techniques. The most accuracy can be obtained by Coordinate Measuring Machine (CMM), which measures an object with a probe sensor touching its surface. But CMMs are very expensive and slow especially for complex surfaces (Carbone et al, 2001).

In addition to contact CMM, there are non-contact approaches widely applied in engineering such as structured light, time of flight (TOF), computer tomography (CT), and active stereovision. The general idea is to project their own energy source to an object, and then observe either the transmitted or the reflected energy (Park and Desouza, 2004).

Among these active techniques, the structured light method is most used in 3-D measurement. The method projects a light pattern (spot, strip, grid or more complex shape) at a known angle onto an object. A camera is used to view this illuminated scene. Through analyzing the reflected light patterns in the images, the 3D information of the object can be acquired (Klette et al, 1998). Unlike passive stereovision, the structured light system can totally avoid the correspondence problem by replacing one camera with a light pattern projector.

2.3 The Slit Laser Scanner

The slit laser scanner is one of the structured light methods. It is a very popular triangulation-based digitizer in 3-D surface reconstruction due to its optical and mechanical simplicity and cost (Blais, 2004). Its basic structure consists of a laser projector and a moving stage as shown in Fig. 2.2.

Rather than using multiple stripes or patterns simultaneously projected onto the object, this method mechanically scans a laser line on the scene, so that the dense and accurate 3D data can be obtained. While scanning, a CCD camera captures the corresponding sequence of images. Through image processing, the illuminated pixels caused by intersection between laser plane and the object are extracted. With the triangulation formula determined by calibration, the 3-D position of corresponding points of the object is computed.

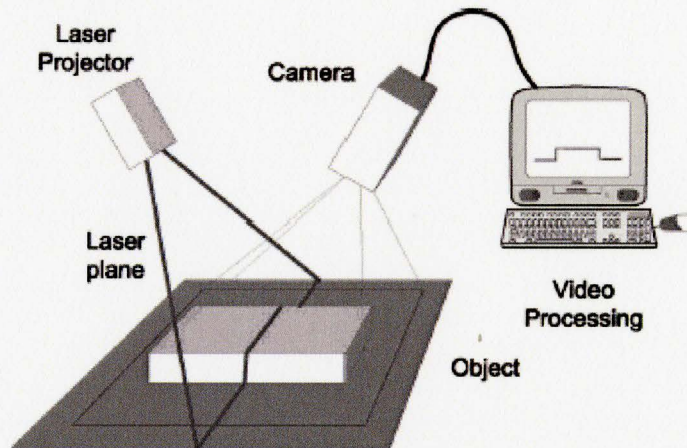


Figure 2.2: A typical slit scanner configuration (Blais, 2004).

However, when designing a slit scanner system, two existing limitations should be considered. One is the limited field of view. This is because the achievement of the large depth resolution is made by way of sacrificing the view of a camera. Generally, 20-30 degree between the camera and laser are applied. Another is the effect of the changing lighting conditions particularly outdoors. It is obvious that strong ambient light will increase the noise of optical measurement no matter what narrow -band optical filter is

used (Blais et al, 1988).

Related with the accuracy of 3-D measurement, there are two problems that need to be resolved:

- Laser stripe detection and
- Calibration.

2.3.1 Laser Stripe Detection

In a 3-D vision system using the slit scanners, the measurement accuracy is significantly determined by the detection of the stripe location in the image (Trucco et al, 1998). Based on the principle of optical triangulation between laser scanner and camera, when a spatial volume is projected onto the image plane, each 2-D point on the image plane should be in correspondence with a 3-D position in space. But for CCD sensors, the integer coordinates denoted by pixels records the information from a range of positions. Thus, in order to enhance the accuracy of 3-D coordinates transmitted from 2-D image coordinates, the peak image position of laser stripe needs to be considered to sub-pixel accuracy (Fisher and Naidu, 1991).

- Laser stripe segmentation

However, before locating the sub-pixel stripe peak, the primary task is to segment the laser stripe. The image processing for it is very complicated especially with the absence of optical filtering in the CCD camera (Strobl et al, 2004). The first point to be considered is the adjustment of some physical parameters of the camera such as focus, hue, brightness and saturation. Next, the background needs to be subtracted to estimate

the rough position of stripe. Strobl used a Sobel filter to detect the edge of stripe. The resultant stripe would be accepted if the color and width of their pixels are within a certain bandwidth determined by the on-line lookup tables. According to his report, this method copes very well with the problem of specular reflections and changing lighting conditions. But a drawback is that large lookup tables need to be made online. The efficiency of this approach may not be very good.

- Sub-pixel peak detection algorithms

A lot research has been published on peak pixel detection. Most methods assume that the observed stripe is wider than 3 pixels; the peak position appears at the zero-crossing of the first derivative of intensity function interpolated with these three or more pixels. Based on this assumption, Fisher and Naidu (1991), and later Trucco et al (1998) tested and discussed five algorithms including Gaussian approximation, center of mass, linear interpolation, parabolic estimator, and Blais and Rioux detectors.

The experimental results from both research teams concluded that the Gaussian approximation method can provide a relatively good and reliable performance especially when the noise level or stripe width decreases. The disadvantage is among these methods the Gaussian is slowest in computation time. However, due to the fast processing speed of the desktop computer the Gaussian method computing time becomes unimportant.

2.3.2 Calibration

In order to reconstruct the depth from an extracted laser stripe, the optical transformation matrix from 2-D image coordinates to 3-D world coordinates must be

determined. A variety of calibration methods have been proposed to estimate the parameters of the transformation matrix. In general, they can be divided into model-based calibration methods and direct calibration methods (Wang et al, 2005).

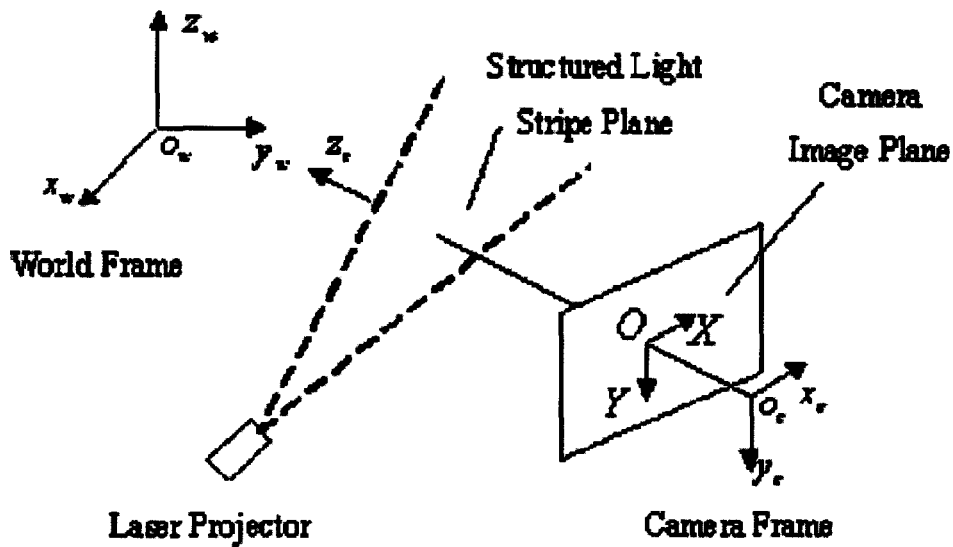


Figure 2.3: A projective model of a structured light (Wei et al 2003).

Fig. 2.3 shows a projective model for the first category. Classically, two separate steps are taken for this model: camera calibration and laser projector calibration (Strobl et. al, 2005). The first step aims to recover the camera's intrinsic and extrinsic parameters. Tsai's nonlinear approach (Tsai, 1987) and Zhang's flexible technique (Zhang, 1999) are commonly adopted in practice and the precise parameters can be achieved with them. The second step is to find the position of the laser projection plane with respect to the world coordinate system. The problem in this step is that the 3D-to-2D point pairs for the calibration are not easily obtained. This is because the known world points on the calibration target may not fall onto the laser stripe plane. There are many solutions to this

problem such as known world line method (Chen and Kak, 1987), zigzag target method (Liu et al, 1999) and Invariant cross ratio (Huynh et al 1999, Wei et al 2005). However, these methods are low in the measurement accuracy due to the limited number of calibration points.

An easy and fast method was presented by Fei and Bin (2004). A planar chessboard is used as a calibration target. First, the camera's parameters are estimated by Zhang's technique. Then, by moving and rotating the chessboard under the structured light, two more intersection lines of the projection plane can be determined with the extrinsic parameters in camera coordinates system. Thus, the projection plane can be positioned by fitting these laser lines. The accuracy this method can reach is about 0.1mm. But modeling a camera is still a tedious and unstable process due to changeable sensor phenomena like focus, and distortion coefficients.

In 1999, Trucco first devised a direct calibration method to reduce modeling difficulty. The principle of his method is to immediately measure the image coordinates of a grid of many known 3-D workspace points, and then establish a grid index lookup table by interpolation to link pixels to 3-D points. This method does not need to estimate the camera and projector parameters. The only problem in the measurement accuracy is the repeatability of the equipment and of the stripe detection algorithm. However, a precise block consisting of 145 steps (each 2mm in length and 1mm in height) is needed for the calibration. Although his report did not mention how to make this block, the cost and time creating it would be high compared to other methods.

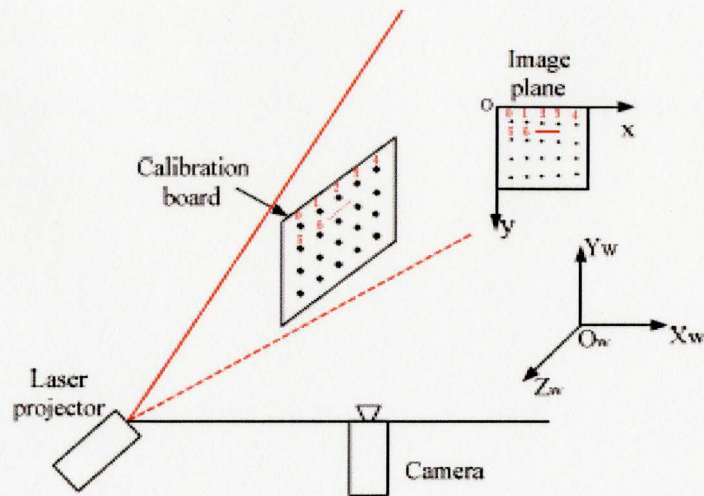


Figure 2.4: The principle of the direct calibration method by Wang et al (2005).

Another report by Wang et al (2005) presented a more convenient and low-cost direct calibration method. A planar calibration board containing a grid of known 3-D points is laid in the plane of laser projection in the workspace as shown in Fig 2.4. Therefore, the point pairs of the 2-D image and 3-D world coordinates are easily recorded. And then by interpolation the coordinates of other points can be obtained. The same idea was also used by Park and Desouza (2004). The difference is they use 2D-3D point pairs to directly compute a 4×3 image-to-world transformation matrix with the least squares method. But the accuracy of these two methods mainly depends on a good coplanarity of the calibration board and the projection plane. In practice, it may take a long time to align them within an accepted accuracy.

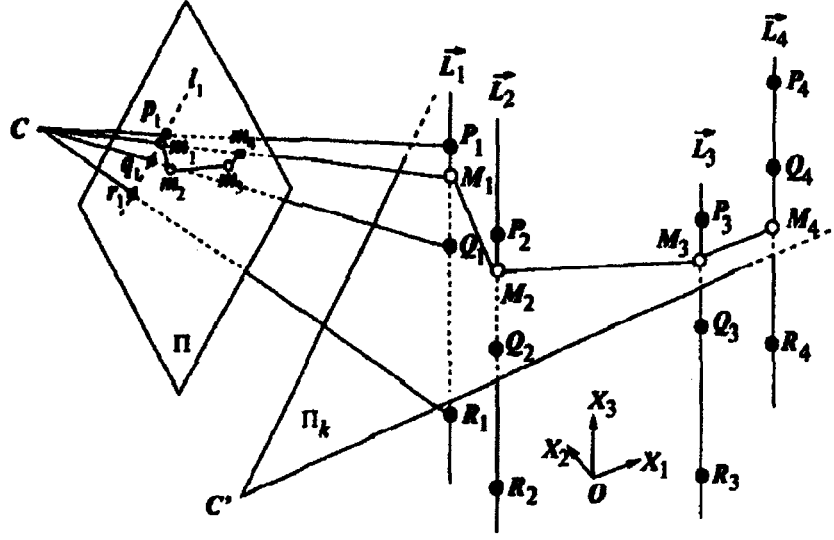


Figure 2.5: Huynh's calibration method (1999). Here Π is image plane, Π_k is projection plane, and C is projection center (focal point of camera).

Different from the methods discussed above, Huynh proposed a calibration method based on calculating the homography matrix from the image plane to the projection plane (Huynh et al, 1999). This homography is obtained from point to point correspondence. In his method, the means of invariant cross-ratio (CR) under projective transformations is employed to acquire these corresponding points. As shown in Fig 2.5, four pencil lines ($\bar{L}_i, i=1\dots 4$) are used as the calibration target, on each of which three world points ($R_i, Q_i, P_i, i=1..4$) are known, so that when the cross-ratio of four points is computed in pixels on the image (e.g. in the line \bar{L}_1 and its image l_1 ,

$$CR(p_1, m_1, q_1, r_1) = \frac{p_1 q_1 / p_1 r_1}{q_1 m_1 / r_1 m_1} = CR(P_1, M_1, Q_1, R_1) = \frac{P_1 Q_1 / P_1 R_1}{Q_1 M_1 / R_1 M_1},$$

points ($M_i, i=1..4$) on the laser stripe can be extrapolated.

In this way, four more non-collinear laser stripe points are obtained, and used to

determine the homography and the pose of projection plane in the world coordinates system. The advantage of this method is the sensor parameters implicitly are accounted for by the straightforward projective transformation matrix instead of mathematically modeling. However, as discussed before, more point pairs need to be obtained in order to improve the calibration accuracy.

2.4 View Registration

In order to model the entire surface of the object, the surface points from different viewpoints need to be obtained. But the problem is the registration of these views. The Iterative Closest Point (ICP) algorithms (Besl and McKay, 1992) are commonly used by many researchers. It is an iterative algorithm for registering two data sets. In each iteration, it selects the closest points between two data sets as corresponding points. A rigid transformation is computed to minimize the distances between corresponding points. The data set is updated by applying the transformation and the iterations continue until the error between corresponding points is below a preset threshold. This method is precise and reliable, but the iteration makes it a tedious and time-consuming process.

In a vision system containing a robot, 360 degree cylindrical scanning is often applied in place of multi-view linear scanning (Chen et al, 1987). The transformation matrix is easily obtained from the robot controller. Besides the short processing time, another advantage is to reduce the registration error which inevitably exists in ICP algorithms. The accuracy of this method is mainly dependant on the accuracy of the robot movement.

2.5 Shape Reconstruction

In computer vision, there are many techniques used for 3-D shape reconstruction: B-splines, surface patches, volumetric descriptions and finite element models. But under forging conditions, surfaces of a workpiece are generally rough and irregular, which would complicate the application of these techniques for geometry measurement. In an algorithm proposed by Goldstein and Wright (1985), the contour of the silhouette at the certain length of the forging is processed to form the cross-section shape. By calculating all the cross-sections along the length of the workpiece, the three-dimensional geometry of the part can be successfully reconstructed. But this vision system needs to move and rotate the part in 360 degree all the way until the whole length of the part is checked. Thus, large running time is expected in the apparatus movements and complicated reconstruction algorithms. The working efficiency of this system is doubted.

2.6 Summary

Previous researches in computer vision provide the substantial knowledge and techniques for the problem of the real-time measurement in the intelligent open die forging system.

Concluded from the literature above, the laser slit scanner is expected to be an effective method in 3D vision system setup due to its simplicity, accuracy and low cost. The rest of this thesis will describe the development and experiments of this system.

Chapter 3

Methodology and System Design

In this thesis, a 3-D vision measurement system in real time is built up for the intelligent open die forging center which is based on Nye's control closed loop and was initially integrated by Li Ma (2004). This vision system follows the general principle of active vision techniques and is specifically designed for the purpose of automatic measurement under forging conditions. The theory and methodology for designing it will be given in this chapter.

The architecture of this vision system has been shown in fig. 1.2. It simply consists of a CCD camera and a slit laser projector. A 6-axis Kawasaki JS6 robot is used to implement the scanning movement. The techniques of image processing, calibration and scanning scheme, all of which are used to determine 3-D locations of the entire surface points of a workpiece, are developed in the following sections before a reconstruction algorithm is programmed to create the cross section at any place along the rotational axis for shape error detection in the last section.

3.1 System Setup

In this thesis, a linear structured light is applied to set up a vision system. The technique employs a CCD camera and a slit laser projector to create a well-known optical triangulation relationship to determine 3-D coordinates of a point with respect to the reference system. A Kawasaki JS robot is controlled by a C++ program to manipulate the workpiece and perform the real-time measurement. The functions and connections of hardware in the vision system are described in this section.

3.1.1 Arrangement of a Camera and a Laser Projector in a Rigid Frame

A 3-D triangulation for the linear structured light is shown in Fig. 3.1, where a camera centered XYZ coordinates system and an image plane lying at $Z=f$ are assumed (Klette et al, 1998). $P(x, y)$ is the image coordinate of a illuminate point $P (X_0, Y_0, Z_0)$, b is the base-line distance from the focal point O to the laser projector along the X axis. α and β are the projection angles between the laser beam and the base line in 3-D space to determine the position of P .

According to the ray theorem, the following equations can be obtained:

$$\frac{X_0}{x} = \frac{Y_0}{y} = \frac{Z_0}{f} \quad (3.1)$$

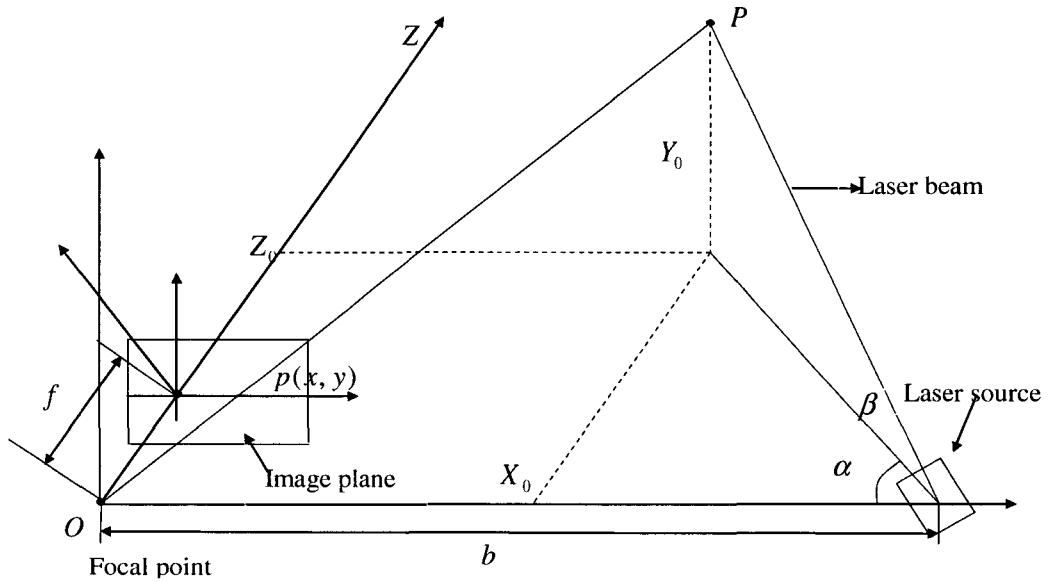


Figure 3.1: A 3D triangulation of a linear structured light system.

Using the notation in Fig.3.1, the trigonometry of the above determines,

$$\tan(\alpha) = \frac{Z_0}{b - X_0} \quad (3.2)$$

From equation 3.1 and 3.2, the 3D position of point P can be calculated by

$$X_0 = \frac{\tan(\alpha) \cdot b \cdot x}{f + x \cdot \tan(\alpha)} \quad (3.3)$$

$$Y_0 = \frac{\tan(\alpha) \cdot b \cdot y}{f + x \cdot \tan(\alpha)} \quad (3.4)$$

And,

$$Z_0 = \frac{\tan(\alpha) \cdot b \cdot f}{f + x \cdot \tan(\alpha)} = \frac{b \cdot f}{f \cdot c \tan(\alpha) + x} \quad (3.5)$$

The depth measurement error ΔZ can be calculated by differentiating the equation (3.5),

$$\Delta Z = \frac{fb}{(x + f \cdot c \tan(\alpha))^2} \Delta x + \frac{fb(f \cdot \csc(\alpha))}{(x + f \cdot c \tan(\alpha))^2} \Delta \alpha \quad (3.6)$$

Where $\Delta x, \Delta \alpha$ are the measurement errors of x and α respectfully. Substituting Z_0 so:

$$\Delta Z = \frac{Z_0^2}{fb} \Delta x + \frac{Z_0^2 \csc(\alpha)}{b} \Delta \alpha \quad (3.7)$$

Indicated from this equation, the depth error is proportionally increased with the square of the depth Z_0 , and decreased with the focal length f and the base-line distance b . Although a large base line can lead to more accuracy of the system, the occluded area due to the shadow effect may not be detected by laser beam. A false measurement would occur. Therefore, when arranging the laser projector and the CCD camera in a rigid frame, the tradeoff between the length and the view of camera needs to be considered (Park and Desouza, 2004), as shown in Fig. 3.2.

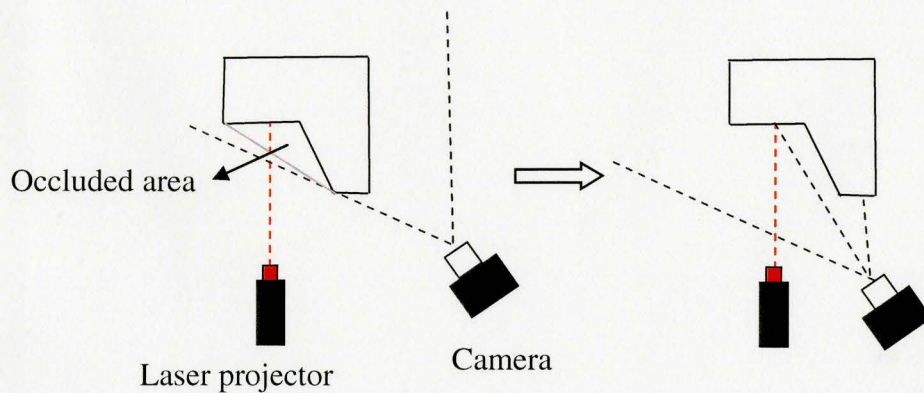


Figure 3.2: Trade -off between the length and the view of a camera.

Another problem in the rigid frame design is the direction of the laser beam. In experiments, a shiny aluminum bar is used for measurement. From some views of the camera, the ambient light may cause a surface point which does not belong to the reflected line to be much brighter than the laser stripe points. In order to make the true illuminated pixels have the strongest intensity value among either a width of laser stripe or the rest of the surface of the aluminum bar, the laser beam is better directly projected onto the object and viewed to be nearly vertical in the image plane. Also because this rigid frame is placed in an open environment, the laser beam is demanded to impinge only onto the measured workpiece and not other objects in a scene captured by the camera, so that the erroneous measurements can be avoided. As a result, the placement of the rigid frame needs to be appropriately adjusted to satisfy the factors above.

Based on the explanations above, the rigid frame of a camera and a laser projector is placed as shown in Fig. 3.3.

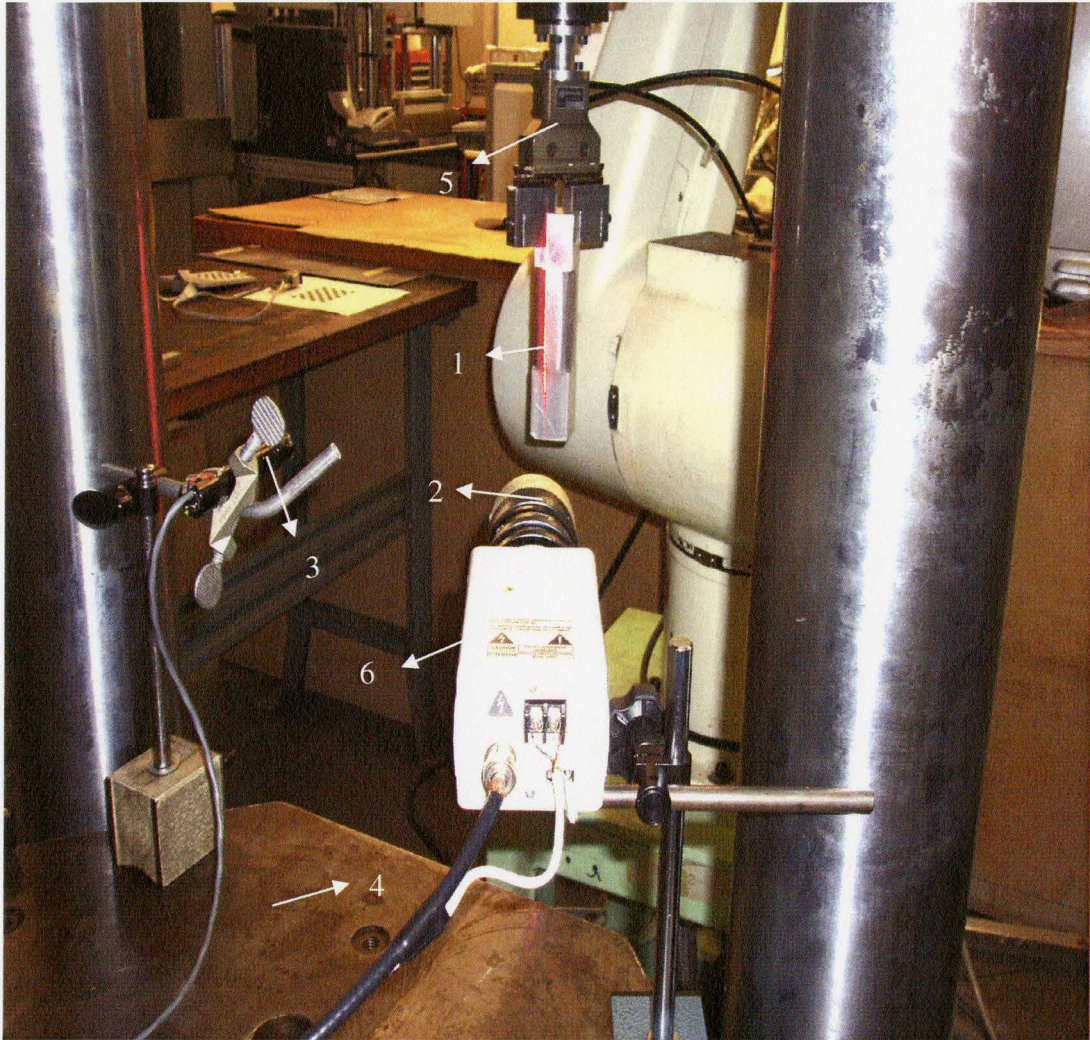


Figure3.3: The rigid frame of a CCD camera and a laser projector. Here 1 is the workpiece, 2 is the camera lens, 3 is the slit laser projector, 4 is the working table, 5 is the gripper, and 6 is the CCD camera.

3.1.2 Hardware Description

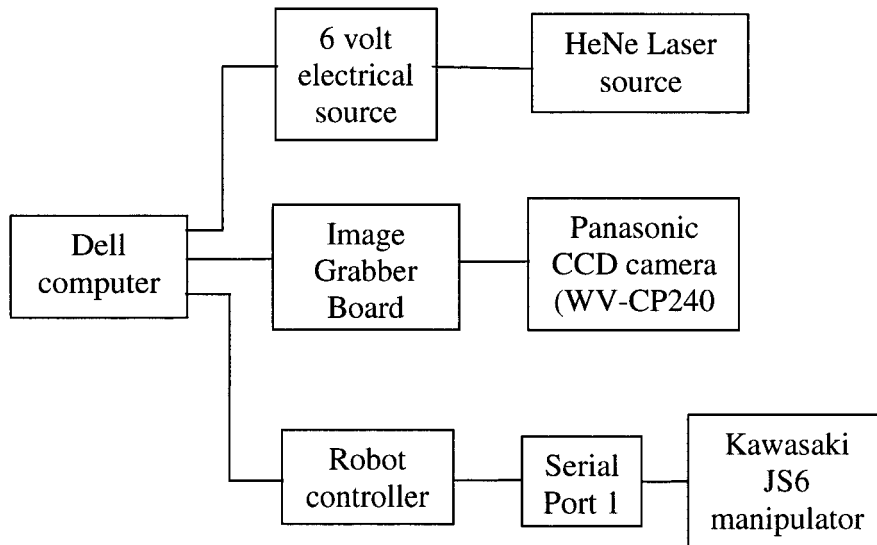


Figure 3.4: Hardware connections of the vision system.

Once the rigid frame is fixed on the working table, the scanning process is carried out by a Kawasaki JS6 manipulator moving a workpiece through a laser projection plane which is obtained by using a HeNe source (output power 500mw at wavelength 400-700nm), mirrors and a cylindrical lens. The laser light is a beam of circular cross-section with Gaussian intensity profile before passing through the cylindrical lens, which spreads the beam into a thin plane. A six volt electrical source provides the power for projecting a laser beam onto the workpiece. The illuminated scene is captured by a Panasonic CCD camera (WV-CP240). A National CCTV zoom lens is installed on the camera. Its focal lens is from 12.5mm to 75mm. A Meteor214 board by Matrox, which is connected with the camera, is used to acquire digital images into the computer. In the

way of using a red laser projection, the form factor of the board is set to be NTSC mode so that a RGB color image can be grabbed. The manipulator is controlled by the computer by way of communicating with the robot controller through a serial cable. The whole hardware connection of the vision system is shown in Fig. 3.4. All the components are linked with a Dell computer and integrated into a C++ control program.

3.1.3 Kawasaki Six-Axis Robot Control

In this vision system, the positions of a Kawasaki six-axis robot need to be programmed for conducting measurement and calibration process. The robot movement strongly determines the measurement accuracy. In this section, the robot control is introduced.

This robot is an industrial arc welding robot and controlled by an AD series controller with two working modes: “Teach Mode” and “Repeat Mode” (Kawasaki Robots (USA), Inc., 1995). In teach mode, the robot can be manually moved by a teach pendant (a remote operation device) and all the positions of the robot are monitored by the program which is built in the controller, and saved in the controller’s memory. In repeat mode, the robot motions are controlled by the program defined by AS language programs or commands. AS (Advanced Superior) language is a computer based control system language specially designed for the Kawasaki robots with an A or AD series controller (Kawasaki Robotics (USA), Inc., 2001). Since a control program is written with it, the robot tasks can be easily defined.

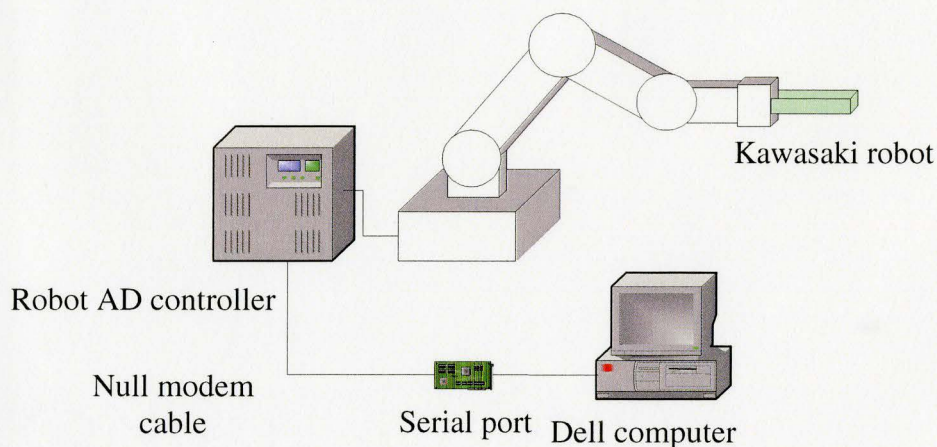


Figure 3.5: Communication between the robot controller and the computer (Ma, 2004).

The communication of the devices is shown in Fig. 3.5. A null modem cable is used between the serial port installed in the computer and the robot AD controller. In repeat mode, the AD controller receives and sends AS commands as strings from or to the serial port. Then the motors in the robot are actuated by those AS command to execute robot motions. In this way, with some basic AS commands, the complex robot motions can be programmed. In this thesis, a function `send_receive()` coded with C++ language is used to monitor the serial communication between the computer and the AD controller by sending and receiving strings. With this function, AS command strings are generated and sent to the controller, and also the strings from the controller are interpreted, so that the robot movement defined by robot joints coordinates or by XYZ coordinates is controlled. The flow chart of this function is shown Fig.3.6.

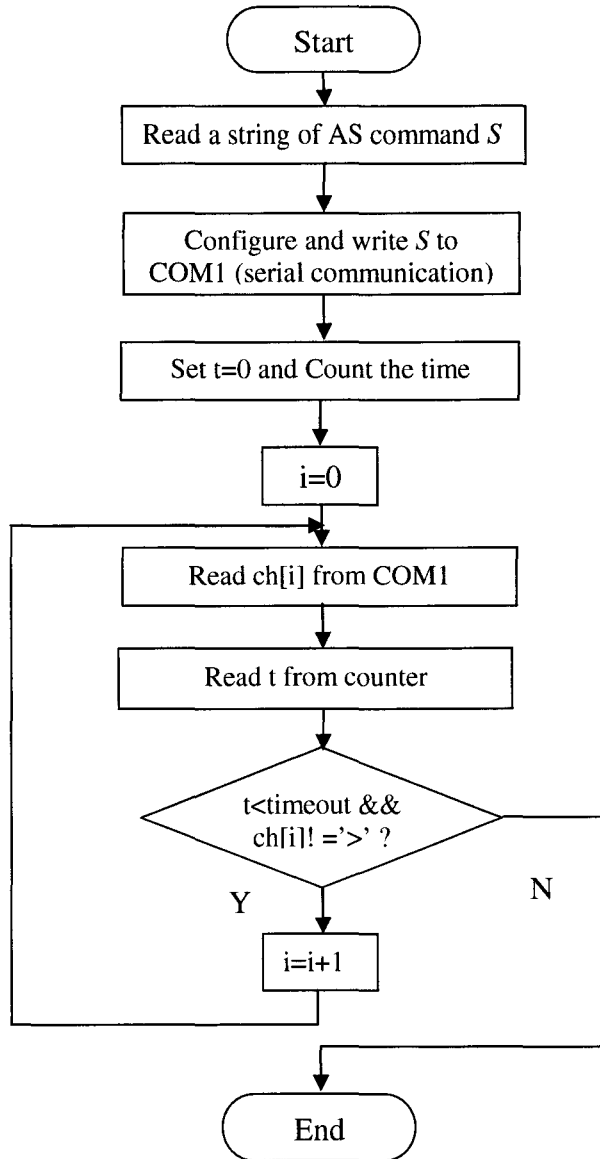


Figure 3.6: The flow chart of function send_receive().

3.2 Laser Stripe Segmentation

When using structured light techniques, a decisive factor in ranging accuracy is the segmentation of the laser stripe projection (Strobl et. al, 2005). The center points of the red laser stripe in a scan image need to be detected, since the resulting image coordinates are the principal inputs to the reconstruction process for 3-D positions of surface points.

In this thesis, the vision system is designed to be used in an open environment without using any optical filter. Thus, there is not only a workpiece but also other objects contained in a captured scene. In case that a light saturation or red light source occurs, a simple segmentation algorithm would falsely detect them as the laser projection. Therefore, different measures must be taken to eliminate these erroneous detections.

In following sections, a laser stripe segmentation method is introduced. This segmentation starts with background subtraction. By means of red color detection and thresholds in RGB channels, a width of stripe of illuminant points caused by the laser beam is independently extracted in each row of the image. At the same time, all the background pixels are discarded by setting them to be black.

Assume that the laser projector is the main light source to cause illumination on the extracted stripe in the context of the vision system. Therefore, in a cross-section of the stripe by each row, there exists a peak pixel with strongest intensity value resulting from the intersection of the laser plane with the object surface. Based on this assumption, the algorithm of the stripe peak detection is completed in two steps, one is brightest red pixel detection, and the other is approximate peak estimation in sub-pixel accuracy.

3.2.1 Adjustment of Camera Physical Parameters

Before taking pictures, the camera physical parameters need to be adjusted so that a good optical performance can be achieved. On this matter, the first is the focal length. In experiments, it is appropriately adjusted until the workpiece measured is clearly viewed in an image.

Saturation is most likely for a non-filtered camera when capturing laser reflection. In order to avoid it, the brightness is adjusted to be as small as possible. Correspondingly, the values of the input gain, hue and contrast are also changed so as to reduce the unexpected phenomena like image blur and optical noise. Here are the values of these camera parameters used in the experiment:

$$\begin{aligned} \textit{Gain} &= 21 \\ \textit{Brightness} &= 47 \\ \textit{Hue} &= 50 \\ \textit{contrast} &= 67 \end{aligned} \tag{3.8}$$

3.2.2 Background Subtraction

In this section, an optical filtering algorithm for background subtraction is introduced. With this algorithm, a red laser line contained in the scan image is detected and approximately positioned. The procedure for it is shown in Fig.3.7.

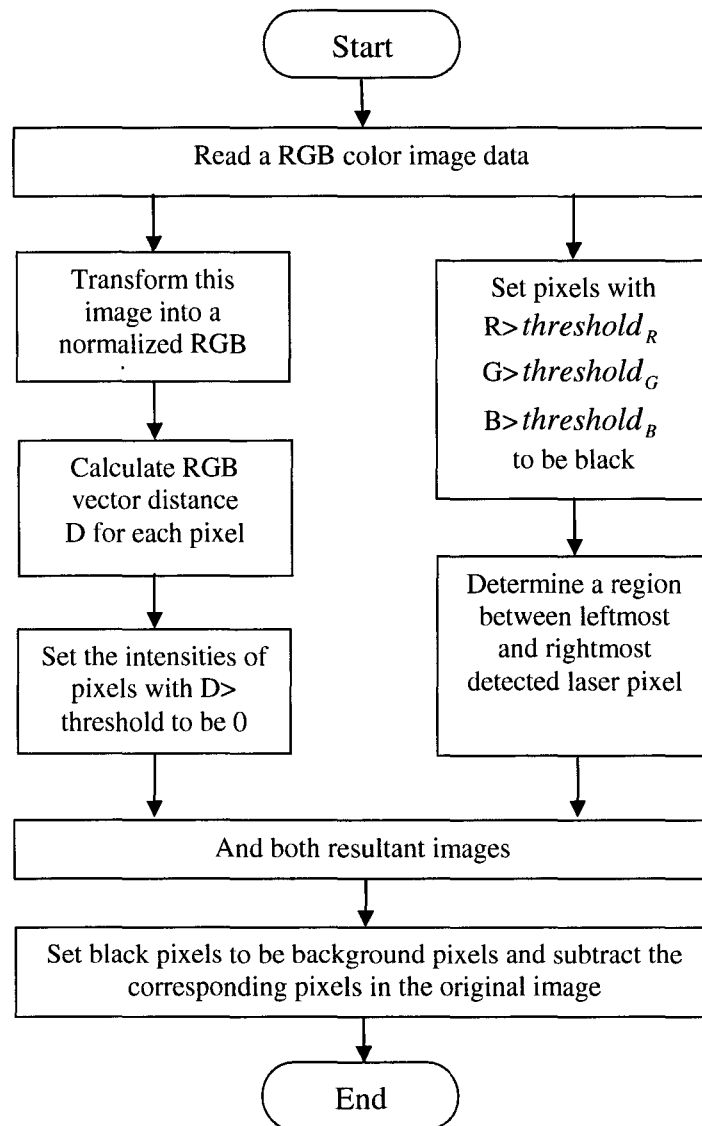


Figure 3.7: Procedure for subtracting background around a laser stripe.

1) Red Color Tracking

Currently, RGB color space is commonly used by most CCD sensors, where each pixel in an image plane has three channels-red, green and blue. With different intensities in three channels of the color image, other colors can be combined. Fig.3.8 below shows a RGB color cube for a uint8 image.

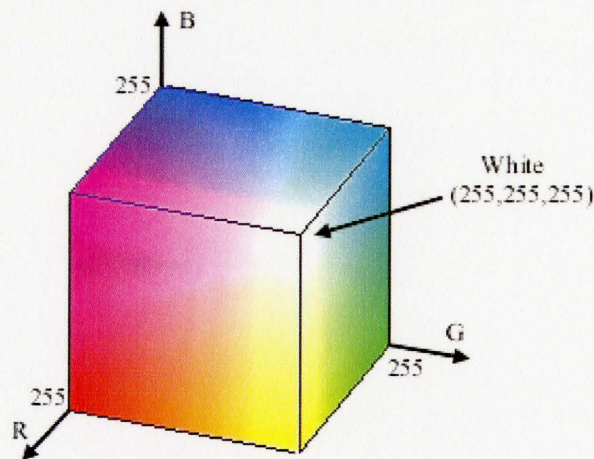


Figure 3.8 RGB Color Cube for uint8 Images.

In RGB space, one of the most popular methods to detect colors is using the vector distance (Slawo and Jernigan, 1999). In the case of searching red pixels, pure red exists when the values of the pixels are:

$$R = 255 \quad , \quad G = 0 \quad , \quad B = 0 \quad (3.9)$$

Though, a tolerance needs to be set, since the laser stripe is not only purely red but also some other red-like color. Suppose that each pixel is a vector:

$$pixel = [R \quad G \quad B] \quad (3.10)$$

The reference color is:

$$RED = [255 \quad 0 \quad 0] \quad (3.11)$$

The Euclidean distance between those 2 vectors is:

$$D = \sqrt{(R - 255)^2 + (G - 0)^2 + (B - 0)^2} \quad (3.12)$$

So any pixel with $D < Theshhold$ (it is 170 in experiment) would be accepted in the filtered image.

But in practice, due to the effect of illumination changes, a raw RGB image is not good enough to detect a certain color. Normalized RGB image transformation is applied to largely avoid this problem. The advantage of this representation is that a normalized RGB is invariant to changes of surface orientation to a light source (Skarbek and Koschan 1994).

2) Normalized RGB Image

Normalized RGB is a representation, which is obtained from RGB, through normalization procedure as:

$$\begin{aligned} r &= R / (R + G + B) \\ g &= G / (R + G + B) \\ b &= B / (R + G + B) \end{aligned} \quad (3.13)$$

In the case of a black pixel, the factor in equation is:

$$R + G + B + 0.1 \quad (3.14)$$

Therefore, in a normalized RGB image, every pixel can be represented by:

$$R = 255 \times r, B = 255 \times b, G = 255 \times g \quad (3.15)$$

After red color tracking, the resultant image is shown in Fig. 3.11.

3) Normalized RGB Image

Although a filtered red color image is obtained, there are still some red pixels not belonging to the laser stripe. Thresholds in three RGB channels of the original image are applied, with which it is easy to determine if the laser stripe exist in the image and where it is located.

Under a certain illumination condition, the laser stripe reflected on objects can be sensed in a narrow range of light spectrum by the camera. The inequations to detect this range are:

$$\begin{aligned} \text{Pixel}_{\text{red}} < \text{threshold}_{\text{red}} \ \&\& \ \text{Pixel}_{\text{green}} < \text{threshold}_{\text{green}} \ \&\& \\ \text{Pixel}_{\text{blue}} < \text{threshold}_{\text{blue}} \end{aligned} \quad (3.16)$$

The preset thresholds are picked with:

$$\begin{aligned} \text{threshold}_{\text{red}} &= 190 \\ \text{threshold}_{\text{green}} &= 200 \\ \text{threshold}_{\text{blue}} &= 200 \end{aligned} \quad (3.17)$$

Since an aluminum bar is used in experiment and its surface is specular and shiny,

the detected illuminant points may not be part of the laser stripe. So instead of searching illuminant pixels, the detection algorithm is to determine the region including the stripe, in that the two columns of the detected utmost right and left pixels are set to be the edges of this region. The pixels out of this region are set to be black with zero intensity values.

When the left and right edges of this region are known, extend this region of interest as below:

[Left edge column -10 pixels, Right edge column +10 pixels]

The reason to do that is to guarantee all the pixels of a laser stripe are included in this region of interest without prior knowledge of the laser stripe. The threshold image is shown in Fig. 3.12.

4) Final Filtered Image

Let

Filtered red color image **AND** Threshold image

The resultant image is shown in Fig.3.13, in which a width of a laser stripe is extracted. As a result, with this image, the background pixels in the original image can be distinguished and set to be the zero intensity values. Thus, the final filtered image is achieved and displayed in Fig. 3.14.

5) Observed Peak of Stripe

After laser stripe segmentation, the stripe peak detection is carried on in the red channel of the filtered image. Due to the placement of the camera and laser beam, the

stripe is viewed as an almost vertical curve between two image rows and its entire shape depends on the shape of the object on which the stripe is observed. Since the curve is vertical, the process of searching peak pixels is implemented from left to right in each row of the red channel image along the extracted stripe. With this principle, a planar curve with the strongest red pixels is detected and shown in Fig. 3.15. But because of limited pixel resolution (in this project, the resolution is 640x480), the observed planar curve might not be at the exact location of the stripe peaks.

6) An Example of Laser Stripe Segmentation

Fig.3.9 shows a picture of a captured illuminated scene and Fig 3.10-15 presents the image optical filtering process for laser stripe segmentation.

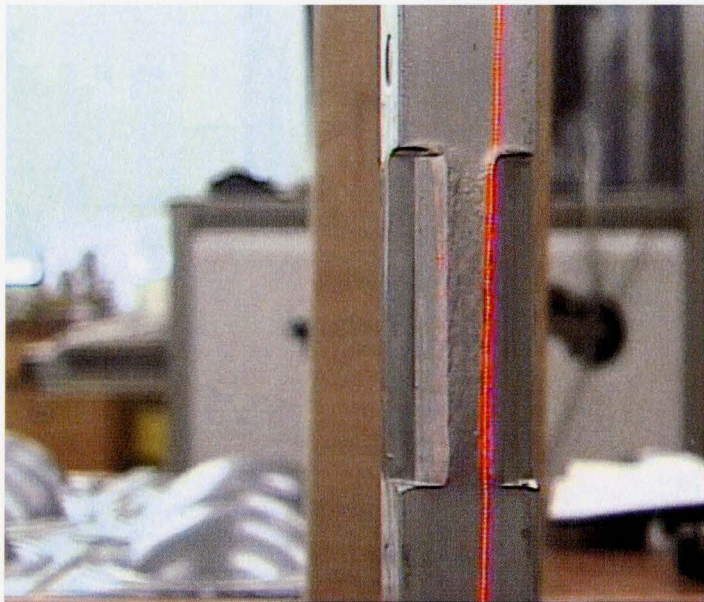


Figure 3.9: A picture of the captured scene.



Figure 3.10: The normalized RGB image.



Figure 3.11: The red color tracking image.

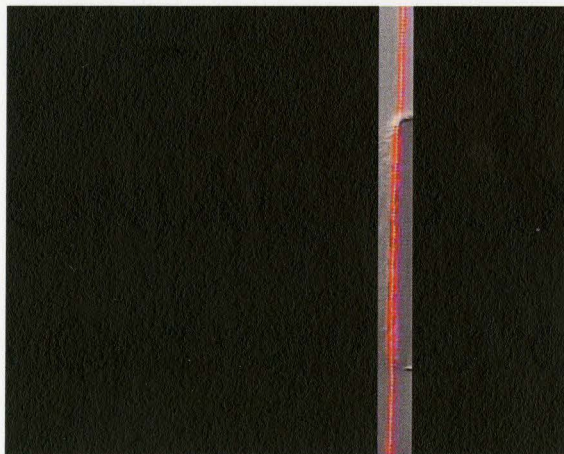


Figure 3.12: A region of interest detected by RGB thresholds.

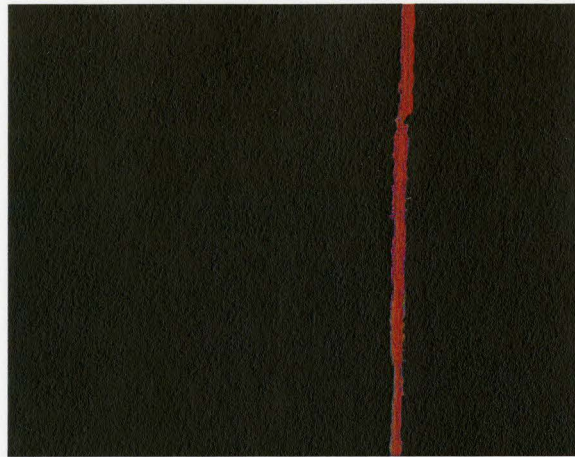


Figure 3.13: The *AND* resultant image.



Figure 3.14: A segmented laser stripe.

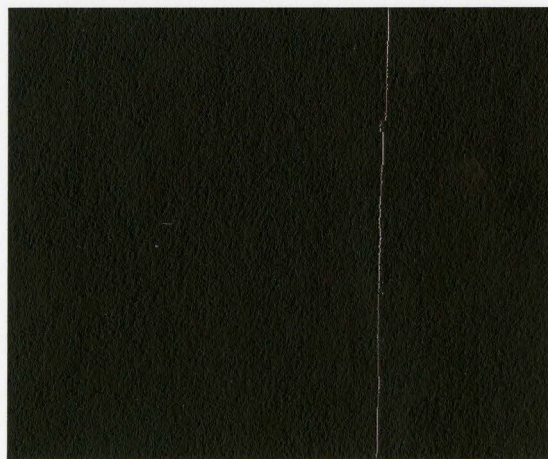


Figure 3.15: Observed peak of stripe.

3.2.2 Sub-pixel Peak Estimation Algorithm

A visual measurement system relies on locational accuracy to the nearest pixel while translating from 2-D camera coordinates to 3-D world coordinates (Fisher and Naidu, 1991). If a large spatial volume of a captured scene is projected onto the imaging surface, each single pixel on the image plane will record information from a range of positions. Thus, the pixel resolution with a discrete representation is limited and not good enough for the precision image analysis in measurement.

As introduced in the previous section, since the observed peak pixel is extracted by a scanning process in each row, the y -coordinate of the pixel is determined by the vertical distance of a column from the top of the image and the x -coordinate is determined by the location of the pixel along a row. Therefore, in this thesis, a continuous x -coordinate is considered so that the true peak positions of a laser stripe can be determined in sub-pixel accuracy.

In this vision system, assume that the laser projector is the main light source to generate the laser stripe on the surface of object and the spread of intensity values (referred to as the sensor response function) across the width of the stripe is not simply random, but conforms to some kind of distribution. For example, an intensity response versus position is presented in Fig.3.16, in which the maximum intensity occurs between the two pixels with the rows of 287 and 288. The distribution among the stripe pixels may be represented by an intensity curve as shown in Fig. 3.17. The point with the zero crossing of the first derivative of this curve would be the approximate peak position. In order to achieve an accurate estimation, it seems reasonable to apply an approximation

algorithm to the cross-section of the strip to compute this zero-crossing point.

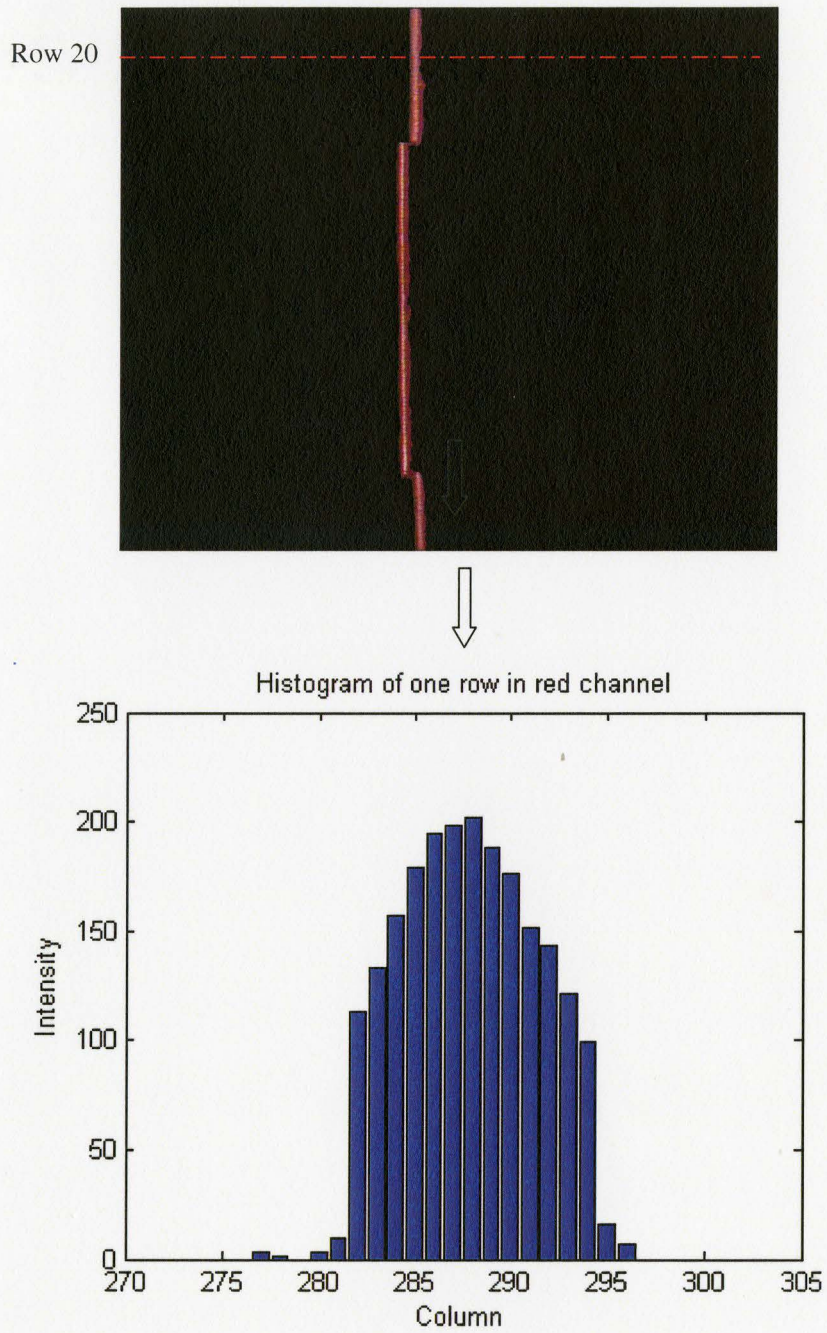


Figure 3.16: Histogram of one row intensities.

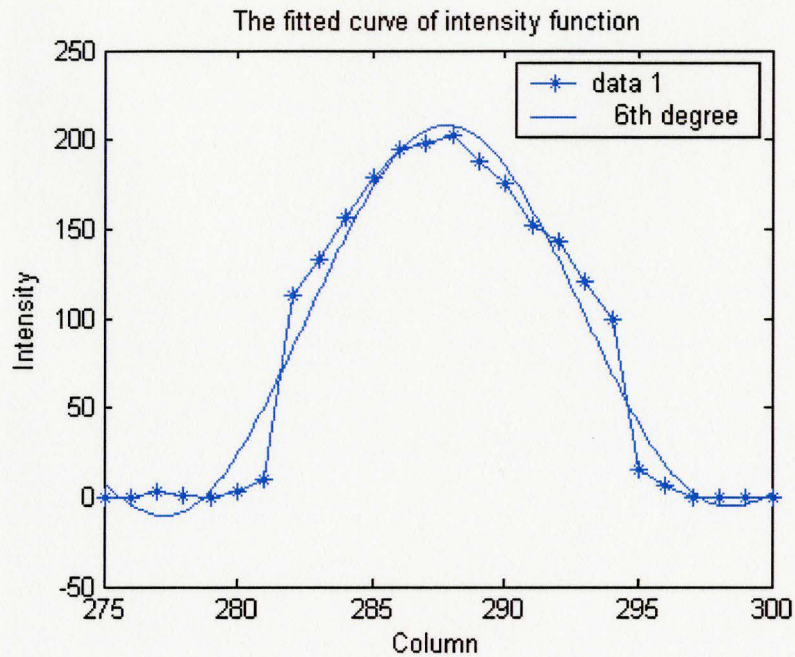


Figure 3.17: A fitted intensity function curve.

Ideally, the intensity function of the laser stripe should in theory be Gaussian. In practice, owing to the CCD camera error (e.g., noise and quantization error) and the imperfections of the laser projector, the Gaussian profile may not be expected (Trucco et al, 1998). For this reason, it is necessary to compare how other non-Gaussian functions fit to the Gaussian one for better performance especially when a shiny or rough forged part is measured. As described in chapter 2, currently, there are five algorithms commonly used to detect laser stripe peaks in sub-pixel accuracy. Center of Mass (COM3) is most commonly applied by other researchers (e.g. Park and Desouza in 2004, Strobl et. al in 2005). In experiments, it and the Gaussian approximation algorithms are tested on an aluminum bar.

In each algorithm, i is the x pixel coordinate with strongest intensity value, $i-1$

and $i+1$ are adjacent pixels, and $f()$ represents intensity value within the integer range 0-255. Then, The sub-pixel location (\hat{x}) of the peak is separately given by:

1. Gaussian approximation. This algorithm assumes that the peak shape fits a Gaussian profile with the three highest, contiguous intensity values around the observed peak of a laser stripe (Fisher and Naidu, 1991).

$$\hat{x} = i - \frac{1}{2} \frac{\ln(f(i-1)) - \ln(f(i+1))}{\ln(f(i-1)) - 2\ln(f(i)) + \ln(f(i+1))} \quad (3.18)$$

When saturation occurs, the measured intensity values of pixels around the peak would have the same value 255. The equation 3.18 will have definite problem in the saturation. Thus, the equation becomes:

$$\hat{x} = \text{Last_overflowed_pixel} - \text{overflow_length}/2 + 0.5 \quad (3.19)$$

In case that the intensity values of two adjacent pixels are equal, the observed peak would be the true one:

$$\hat{x} = i \quad (3.20)$$

2. Center of Mass (COM3). This algorithm also assumes Gaussian distribution of the spread of intensity values across the stripe. The location of the center is computed by weighted average method. It is:

$$\hat{x} = i - \frac{f(i+1) - f(i-1)}{f(i-1) + f(i) + f(i+1)} \quad (3.21)$$

After testing these two methods, the results are comparatively shown in Fig.3.18 and Fig.3.19. It is obvious the laser peak line detected by the Gaussian approximation algorithm is apparently more continuous than Center of Mass especially when measuring a rough surface. Therefore, the Gaussian estimator is applied in this thesis.

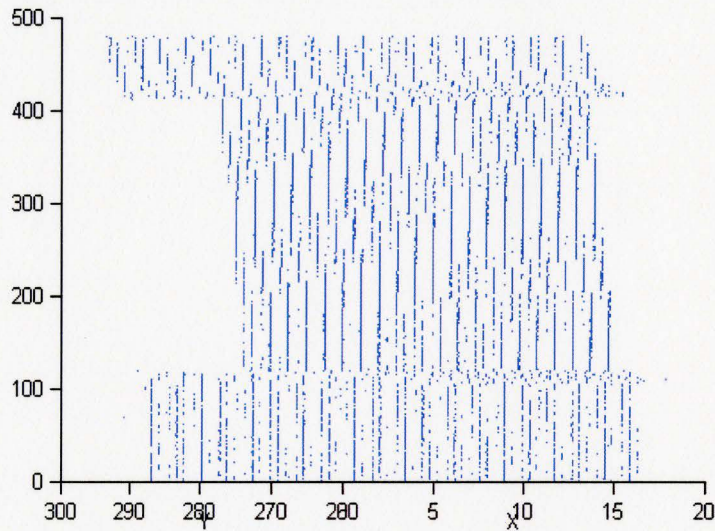


Figure 3.18: The result of Center of Mass.

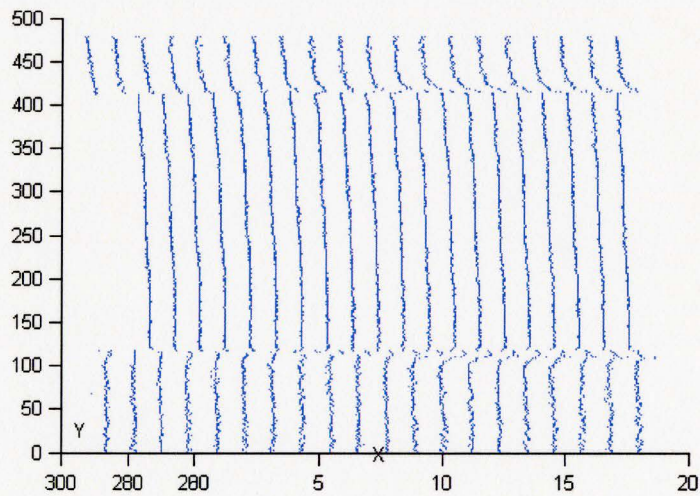


Figure 3.19: The result of the Gaussian estimator.

3.3 Calibration

Range data acquired by a three-dimensional scanner are commonly a cloud of points, which is a discrete approximation of a real object. In a structured-light triangulation system, one of the key factors affecting the accuracy of this digital representation is the calibration method that determines the correspondence from 2-D image coordinate points to 3-D world coordinate points. Most methods are based on building closed-form models of the camera and laser projection. The more precise the geometries of real object are measured, the more parameters are needed to be determined such as the intrinsic and extrinsic parameters of camera and the position of laser projector (e.g., the angle between base-line and the direction of laser beam) (Trucco et al, 1998). A complicated system would be expected in such an approach.

Inspired by Zhang's flexible calibration technique and Huynh's structured light projection model, a simple fast calibration method is proposed. The basic idea of this method is to find the pose of the laser projection plane in the reference system and to map the points in the projection plane onto the image plane by finding the homography matrix between them, so that an image-to-world transformation matrix can be determined. The implementation of this method is introduced in the following sections.

3.3.1 Basic Concepts

- A pinhole camera model with homogenous coordinates

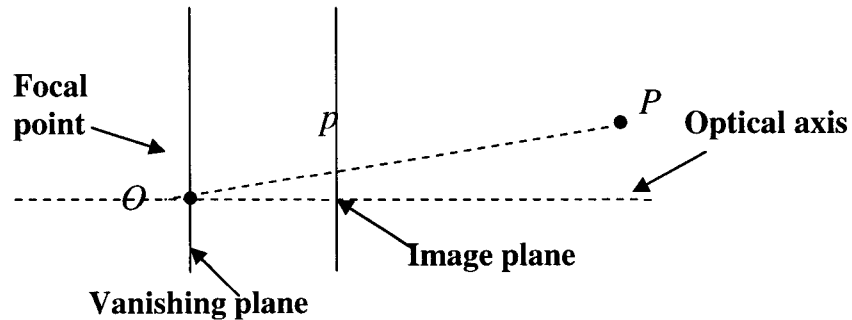


Figure 3.20: A pinhole camera model.

Taking pictures by a camera can be modeled by way of the projective geometry as shown in Fig.3.20, which is often called a pinhole camera model. In this model, the focal point O is referred to as a projection center, through which all rays of light impinging into the camera are projected onto the image plane. The optical axis of the projection is perpendicular to the image plane and passes through the focal point.

A line containing the focal point and an image point can represent a ray of light from a certain direction. All points on the same line are viewed as a single point in the image. The resulting issue is how to transform 2-D image points into 3-D points in projective space in the pinhole camera model (Klette et al, 1998).

With homogenous coordinates, a 3-D point M and 2-D image point m in pixels are separately denoted by:

$$M = [X, Y, Z, 1] \text{ And } m = [u, v, 1] \quad (3.22)$$

The linear projective relationship between them is given by:

$$sm = A[R \ t]M \quad (3.23)$$

Where s is an arbitrary scale factor, A is the camera intrinsic matrix determined by the innate properties of the camera, and $[R \ t]$ called the extrinsic matrix, R is the rotation and t is translation that relates the world coordinate system to the camera coordinate system (Zhang, 1999).

For instance, when a model plane is on $Z=0$ of the world coordinate system, the equation can be:

$$\begin{aligned} s \begin{bmatrix} u \\ v \\ 1 \end{bmatrix} &= A \begin{bmatrix} r_1 & r_2 & r_3 & t \end{bmatrix} \begin{bmatrix} X \\ Y \\ 0 \\ 1 \end{bmatrix} \\ &= A \begin{bmatrix} r_1 & r_2 & t \end{bmatrix} \begin{bmatrix} X \\ Y \\ 1 \end{bmatrix} \end{aligned} \quad (3.24)$$

Where $A \begin{bmatrix} r_1 & r_2 & t \end{bmatrix}$ is considered as a homography matrix between the model plane and the image plane, generally denoted by H .

- Computation of Homography Matrix

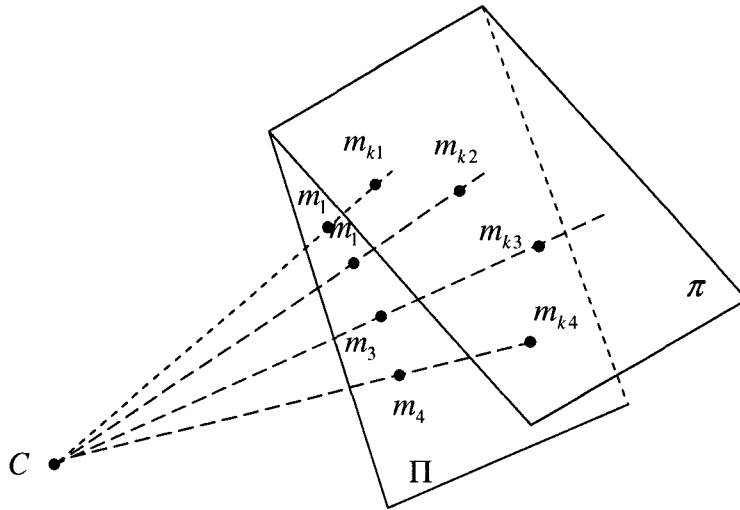


Figure 3.21 Plane to plane homography.

In a 3D projective geometry (in Fig.3.21), the term homography refers to a plane-to-plane transformation in the projective space (Huynh et al, 1999). In Fig. 3.21, given 4 or more points m_i ($i > 4$, no three points are collinear) on plane Π , under a projective center C , there exist the corresponding projective points m_{ki} in another plane π . Their relationship is determined by a unique homography matrix H (3×3):

$$Hm_i = \lambda m_{ki} \quad (3.25)$$

Where λ is an unknown scalar, and

$$H = \begin{bmatrix} h_{11} & h_{12} & h_{13} \\ h_{21} & h_{22} & h_{23} \\ h_{31} & h_{32} & h_{33} \end{bmatrix} \quad (3.26)$$

Induced from the equations above, if at least four pairs of non-collinear points are known, 9 parameters of matrix H can be computed. But in practice, due to the noise in measured points, the equation 3.25 is not ideally satisfied.

There are many ways to estimate the homography between two projective planes. Here, Zhang's technique is introduced, which is based on maximum likelihood criterion (Zhang, 1999).

Denoted in Fig. 3.21, assume that m_{ki} is corrupted by Gaussian noise with mean zero and covariance matrix $COV_{m_{ki}}$, the maximum likelihood estimation of H is obtained by minimizing the following function

$$\Sigma(m_{ki} - \hat{m}_{ki})COV_{m_{ki}}(m_{ki} - \hat{m}_{ki}) \quad (3.27)$$

Where

$$\hat{m}_{ki} = \frac{1}{h_3^T m_i} \begin{bmatrix} h_1^T m_i \\ h_2^T m_i \end{bmatrix}, \text{ with } h_i \text{ the } i^{\text{th}} \text{ row of } H$$

Calculation of this function is complicated. Fortunately the imaging library OpenCV (Intel, 2006), has a function `cvFindHomography` to solve this problem.

3.3.2 Calibration Process Description

The principle of the calibration process is to create a calculation path that allows one to determine the real (X, Y, Z) Cartesian coordinates of a calibration point with the

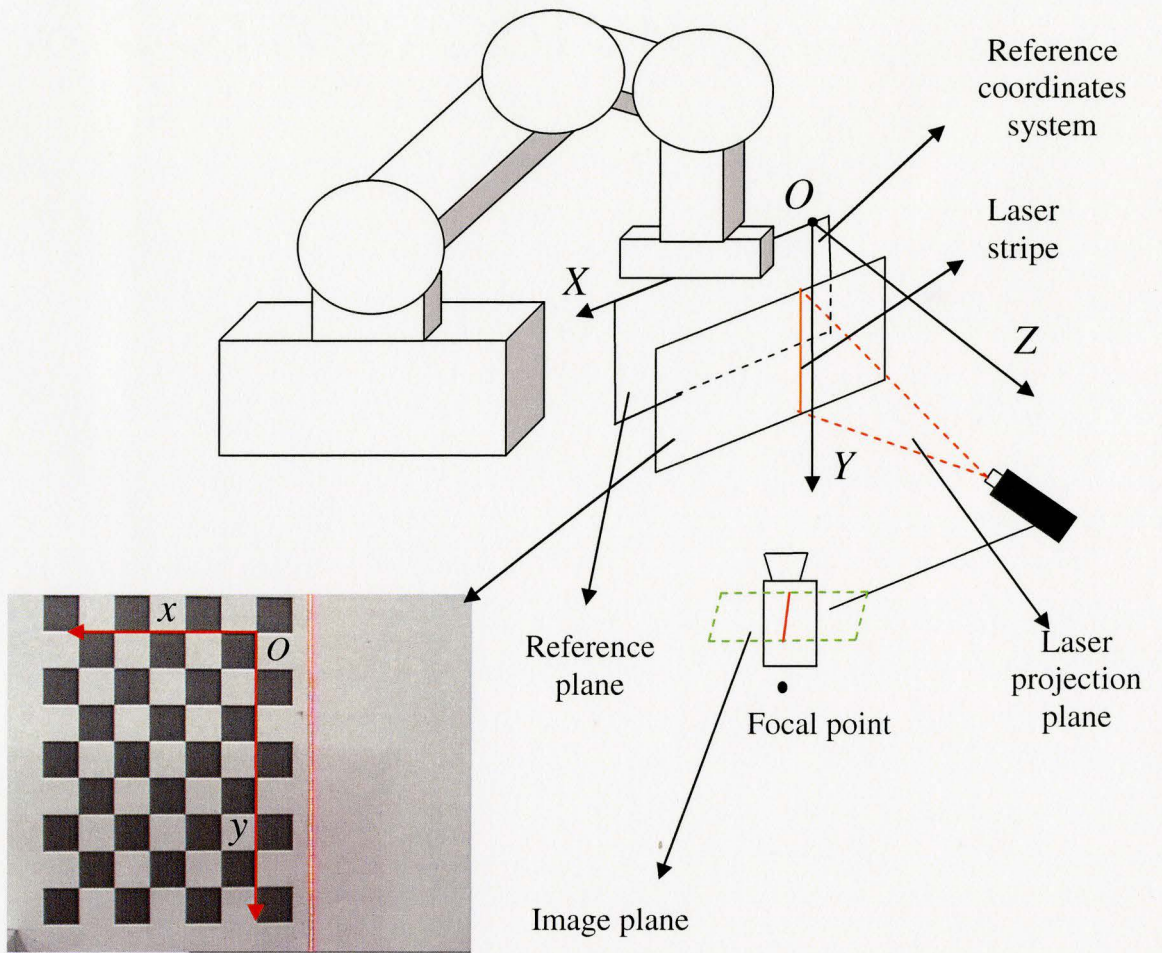
corresponding image pixel without any knowledge of the geometry of camera-projector modeling. The architecture of the calibration system is constructed as shown in Fig. 3.22. The calibration target is a shifting planar chessboard that is denoted as the model plane. At the initial position of the chessboard, assume that the origin of the reference coordinates system is fixed at the top right internal corner of the chessboard, the X -axis is along the second top edge of the chessboard in which the positive direction is from right to left, and Y -axis is along the second right edge of the chessboard positively down to the bottom corner. The resulting Z -axis of the reference system is passing through the origin and parallel to the linear displacement vector of the shifting chessboard. The model plane at $Z=0$ is positioned as the reference plane. A 2-D coordinate frame in the reference plane is merged with the XY axes of the reference system.

The procedure for the calibration is summarized in the following steps:

1. Laser-print a planar chessboard and attach it to a flat surface of a special fixture, which is connected with the 6th joint of the robot.
2. Manipulator holds and shifts the chessboard along the normal vector of the chessboard surface toward the laser projector in sequence to several given positions, where the step between two positions is 5mm. During the calibration process, the laser is always projected onto the chessboard surface.
3. At a position, the controller sends a trigger signal to camera, capturing the illuminated scene. At the same time the chessboard position is recorded.
4. The scene image is processed to extract illuminant point image pixels caused by the laser beam.

5. Locate the corner image coordinates of the chessboard in sub-pixel accuracy. Calculate the homography matrix between the model plane and the image plane by way of Zhang's technique.
6. Compute 3-D coordinates of the laser points with the homography and the shifting position of the model plane.
7. Move to another position, repeat step 3-6. Store 3-D coordinates of the laser points in the reference system.
8. Fit a projection plane with 3D laser points and find the homography between image plane and projection plane using four nonlinear distant point pairs.
9. Find the pose of projection plane with respect to reference coordinates system.
10. Finally, determine the image-to-reference transformation matrix.

The time of the calibration procedure depends on the number of calibrations planes. In experiment, 18 shifting positions are set for calibration and it will take about 5 minutes to finish the whole process. The details are given by the following.



A shifting chessboard denoted by model plane

Figure 3.22: Calibration process description.

3.3.3 Determining Image-to-Model Homography

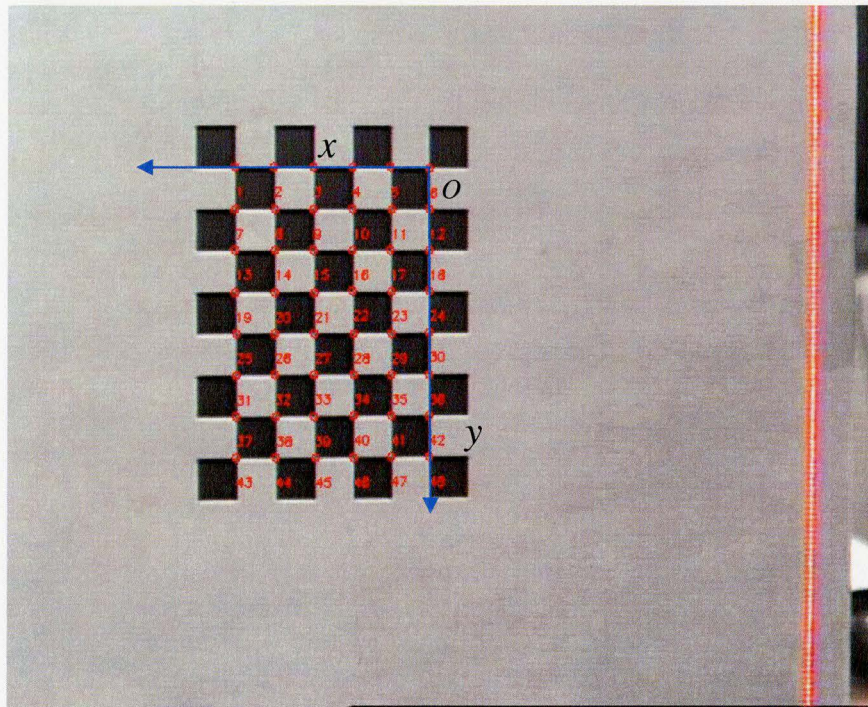


Figure 3.23: Extracted corners in the model plane.

During the calibration, the images of the model plane are recorded by the CCD sensor. A chessboard and a reflected laser stripe can be viewed in each image. Considering working convenience and image processing accuracy, the laser beam cannot be shot across the chessboard pattern.

For each image grabbed at a shifted position, the function ‘cvFindCorner’ in OpenCV is applied to locate internal chessboard corners (Intel, 2006). As shown in Fig. 3.23, there are 48 internal corners found and placed in a certain order (row by row, left to right in every row), where the black squares touch each other. But in this way, the image coordinates detected are approximate, and in order to make their positions more

accurately, the function ‘cvFindCornerSubPix’ is used to determine them in sub-pixel accuracy by an iteration algorithm.

In the model plane, the chessboard is of 7x9 squares pattern. The size of each square is 10x10mm. Assume the corner 6 in Fig. 3.23 is fixed as the origin (0, 0) of 2D coordinate frame. The algorithm below is used to compute the coordinates of other corners:

```
// Determining coordinates of corners in model plane frame
for(i=0;i<8;i++)
{
    for(j=0;j<6;j++)
    {
        M[i*6+j].x=(float)(5-j)*square_size;
        M[i*6+j].y=(float)i* square_size;
    }
}

/* Where M is the corner point, i,j are the row and column
of chessboard pattern. */
```

Figure 3.24: Algorithm of the determination of corner coordinates in model plane.

With these pairs of projective points on the model plane and the image plane, the homography matrix can be obtained by means of the method described in section 3.1.2. Therefore 2-D coordinates of any point in the model plane will be given by:

$$\begin{bmatrix} \bar{x} \\ \bar{y} \\ \rho \end{bmatrix} = H^{-1} \begin{bmatrix} u \\ v \\ 1 \end{bmatrix}$$

$$x = \bar{x} / \rho, y = \bar{y} / \rho \quad (3.28)$$

Where ρ is an unknown non-zero scalar, x, y are the 2-D coordinates of a model plane, and u, v are the point image coordinates, H^{-1} is the inverse matrix of homography H .

An example of the experimental result is shown in Fig. 3.25 for comparing the actual corners and the corners calculated with equation 3.28 (Here, the position of the model plane is at $Z=0\text{mm}$).

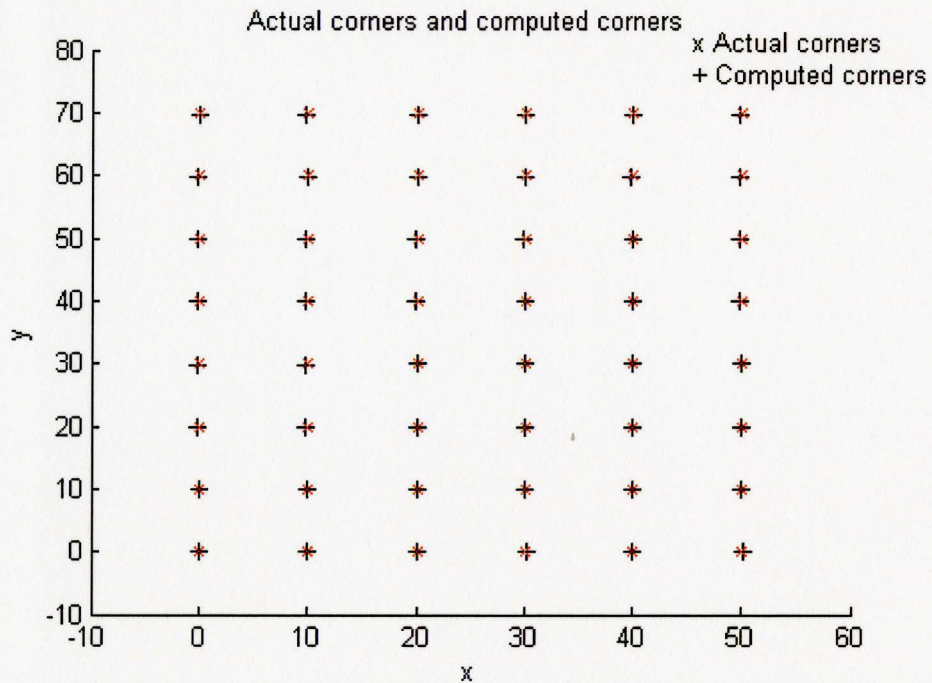


Figure 3.25: Comparison of actual and computed corners (Axis scales in *mm*).

Table 3.1 lists the maximum error, mean square error of x, y coordinates and the deviation distance between the actual and computed corner points. From this table, one can conclude that this method is accurate enough for determining 2-D positions of the points in the model plane. Because in next sections a laser plane including the laser points detected in the model plane is fitted with the least squares method, some measurement

errors in this stage would be relieved.

Table 3.1: The experimental errors when using computed homography matrix

Errors	x (mm)	y (mm)	Deviation distance (mm)
Maximum error	0.2167	0.3327	0.3887
Mean square error	0.0912	0.1646	0.1882

3.3.4 3D Reference Coordinates of Laser Stripe Points in Model Plane

Through image processing in a calibration image, a projected laser stripe in the model plane can be extracted with sub-pixel accuracy. In order to measure the pose of the laser projection plane, 3-D position of each stripe point need to be defined with respect to the reference coordinates system. Since the model plane is parallel to the reference plane and shifted toward the laser projector, the following features are produced:

- (x, y) coordinates of the point in a shifted model plane should be equal to (X, Y) coordinate of the point with respect to the reference system.
- At a shifted position, all the points in the model plane should have the same Z coordinate value with respect to the reference system, which is achieved by the robot displacement and equal to the perpendicular distance to the reference plane.

Therefore, when given a homography matrix between a model plane and the image plane, (X, Y) coordinates of a 3-D laser point is easily computed with equation 3.28. The Z coordinates values of the laser stripe points are obtained from the robot controller and

equal to each other in the same model plane. Thus, the 3-D coordinates of every laser point are determined.

3.3.5 Fitting the Laser Projection Plane

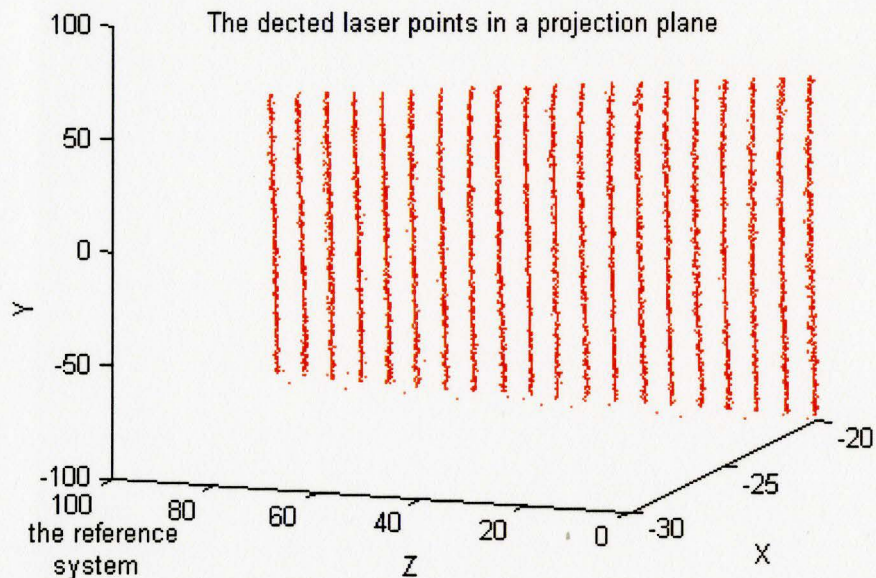


Figure 3.26: The detected calibration points in the laser plane (Axis scales in *mm*).

A quantity of the obtained 3-D calibration points are shown in Fig.3.26 and would in theory be contained in a planar surface. However, in the experiments, due to measurement noise (e.g. false laser point detection and incorrect homography computation), these points may not be exactly coplanar and are not able to directly determine the projection plane. A plane-fitting algorithm with them needs to be applied. In this thesis, the fitting problem is optimally resolved by the Orthogonal Least Squares Fit method (Feng and Hopp, 1991).

This method is also called geometric fit. The idea is to minimize the sum of the squared distances S from the calibration points to the best fitting plane. Suppose there is a point C in this plane, therefore,

$$S = \sum_{i=1}^m ((p_i - C) \bullet \vec{u})^2 = \sum_{j=1}^3 \sum_{i=1}^m [(p_{i,j} - C_j)u_j]^2 \quad (3.29)$$

Here, p_i is the calibration point, m is the total number of points, $\vec{u} = (u_1, u_2, u_3)$ is the unit normal vector of the fitting plane.

Taking the partial of S with respect to C and setting the derivatives equal to zero,

$$0 = \frac{\partial S}{\partial C} = -2 \sum_{j=1}^3 \sum_{i=1}^m (p_{i,j} - C_j)u_j^2 \quad (3.30)$$

Because $\|\vec{u}\| = 1$ and u_n can not all be zero, induced from equation 3.30, the point C is defined by:

$$C = \frac{1}{m} \sum_{i=1}^m p_i \quad (3.31)$$

Thus, equation 3.29 would be,

$$S = \sum_{i=1}^m [(p_i - C) \bullet \vec{u}]^2 = \vec{u}^T A^T A \vec{u} \quad (3.32)$$

Here, $A = \sum_{i=1}^m (p_i - C)$.

If the normal vector \vec{u} is in the same direction with one of the principle directions of the covariance matrix $A^T A$, S would have the extreme value and can be minimized to be the smallest eigenvalue of $A^T A$. As a result, the corresponding eigenvector is regarded

as the estimated surface normal of the fitting plane. Note that both $A^T A$ and A have the same eigenvectors. In practice, to avoid the singular problem and increase the precision, the *SVD* (singular value decomposition) method is applied to resolve this Eigen problem,

$$A = UWV^T \quad (3.33)$$

Here, W is the eigenvalue diagonal matrix, the columns of V are the eigenvectors.

Computing the unit normal to the experiment results from Fig.3.26 gives:

$$\vec{u} = \begin{bmatrix} u_1 \\ u_2 \\ u_3 \end{bmatrix} = \begin{bmatrix} 0.9996 \\ 0.0025 \\ 0.0265 \end{bmatrix}$$

3.3.6 A Model of Laser Projection

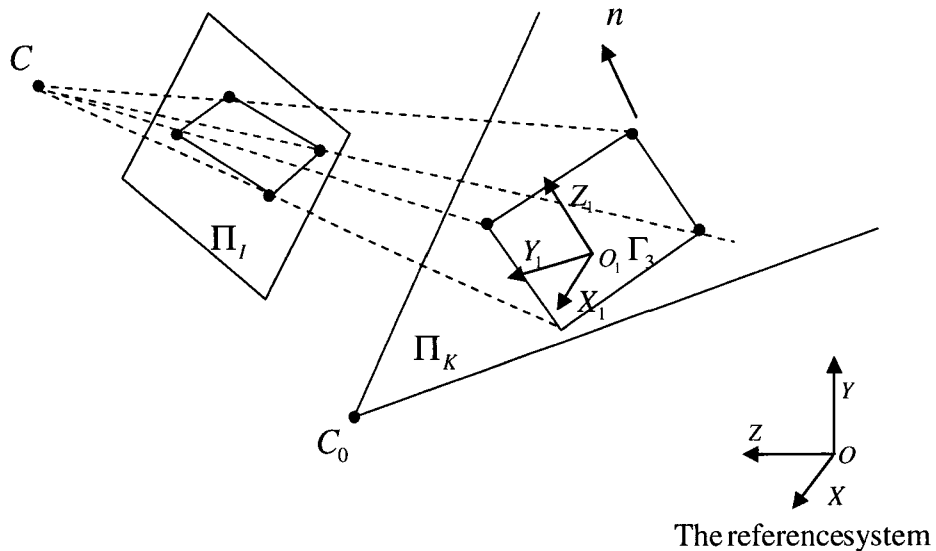


Figure 3.27: A laser projection model.

As shown in Fig.3.27 , the relationships among image plane, laser projection plane and the reference system can be perceived from a laser projection model proposed by Huynh et al (1999). A motivation behind this model is to determine the transformation matrix from image plane to the reference system.

In this model, let Γ_2 be a 2-D coordinate frame lying on the projection plane Π_k . As introduced in section 3.3.1, under a projective center C , a unique homography can be determined by 4 more non-collinear points in general position defined by Γ_2 and their corresponding projective points in image plane. Since the homography exists regardless of the choice of the 2-D coordinate frames in both projective planes, Γ_2 can be arbitrarily defined. To relate the coordinate frame Γ_2 , a 3-D coordinates system Γ_3 is set up, where the X_1, Y_1 axes lie on the projection plane Π_k and the Z_1 -axis is parallel to the normal vector n which is obtained from the previous section. Thus, the two axes of 2-D frame Γ_2 are defined to be coincident with the X_1, Y_1 axis of Γ_3 , but their directions are still unknown in this stage. Based on this model, the image-to-reference transformation matrix can be determined in following.

3.3.7 Determining the Matrix from the Reference System to the Projection Plane

The pose of the projection plane with respect to the reference system is determined by the angle ϖ between the unit normal vector \vec{u} of the projection plane and Z axis (0, 0, 1) of the reference system. It is simply computed by the inner product of the two vectors:

$$\varpi = \cos^{-1}(\vec{u} \bullet (0,0,1)) = \cos^{-1}(u_3) \quad (3.34)$$

Compute the rotation matrix R by aligning Z-axis with the unit normal. This matrix can be derived as follows (Bottema and Roth, 1979):

$$R = \vec{u}\vec{u}^T + \cos\varpi(I - \vec{u}\vec{u}^T) + \sin\varpi(I \times \vec{u}) \quad (3.35)$$

$$I \times \vec{u} = \begin{bmatrix} 0 & -u_3 & u_2 \\ u_3 & 0 & -u_1 \\ -u_2 & u_1 & 0 \end{bmatrix} \quad (3.36)$$

Where \vec{u}^T is transpose of \vec{u} , I is 3x3 identity matrix and $I \times \vec{u}$ is the skew-symmetric matrix. If \vec{u} and Z-axis are parallel then $\varpi = 0$ and $R=I$.

Since the origin $O_1(X_c, Y_c, Z_c)$ of the coordinate frame Γ_3 can be arbitrarily chosen, for convenience in programming, a detected laser point $p(x, y, z)$ is used to determine it. Therefore, X_c, Y_c are x, y coordinates of p, the Z_c can be calculated by the equation 3.29 with x, y .

Thus, the transformation from the reference system to Γ_3 can be regarded as a rotation R around Z-axis and a translation from the origin of the reference system to $O_1(X_c, Y_c, Z_c)$, give the matrix defined as 4x4 matrix T_k :

$$T_k = Rot(\varpi)Trans(X_c, Y_c, Z_c)$$

$$T_k = \begin{bmatrix} R & -RO_1 \\ 0^T & 1 \end{bmatrix} \quad (3.37)$$

The experiment result is;

$$T_k = \begin{bmatrix} 0.17775 & -0.00539 & -0.9841 & -2.8514 \\ -0.0054 & 1 & 0.9841 & 4.0189 \\ 0.9841 & 0.0646 & 0.1774 & -15.6696 \\ 0 & 0 & 0 & 1 \end{bmatrix}$$

Using the form of homogenous coordinates, any world point $M=(X, Y, Z, 1)^T$ lying on the projection plane can be transformed to a point $M'=(X', Y', 0, 1)^T$ with respect to Γ_3 , in that $Z'=0$. It is:

$$T_k M = M' \quad (3.38)$$

3.3.8 Image-to-Projection Homography Matrix

Because the two axes of coordinate frame Γ_2 are defined to be identical to the X_1, X_2 -axes of the coordinate frame Γ_3 , a point m' in Γ_2 can now be directly computed from a world point lying on Π_k by:

$$m' = \begin{bmatrix} 1 & 0 & 0 & 0 \\ 0 & 1 & 0 & 0 \\ 0 & 0 & 0 & 1 \end{bmatrix} T_k M \quad (3.39)$$

Here, define:

$$S = \begin{bmatrix} 1 & 0 & 0 & 0 \\ 0 & 1 & 0 & 0 \\ 0 & 0 & 0 & 1 \end{bmatrix}$$

The method introduced in section 3.1.2 is applied to determine image-to-projection homography matrix. Choosing 4 distant pairs of image and projection points in which no 3 points are collinear, the relationship between them is given by:

$$H_k m = \rho m' \quad (3.40)$$

Where H_k is image-to-projection homography matrix, $m = (u, v, 1)'$ is image homogenous coordinates of a laser point in pixels, ρ is an unknown non-zero scalar.

3.3.9 Image-to-Reference Transformation Matrix

Since T_k is a Euclidean transformation, it is invertible. With the equation 3.39, a laser point m' in projection plane can be transformed into a corresponding 3-D point M in the reference system by:

$$M = T_k^{-1} S^T m' \quad (3.41)$$

Where T_k^{-1} is the inverse matrix of T_k .

Substituting m' obtained from equation 3.40 into equation 3.41, gives:

$$M = T_k^{-1} S^T H_k m / \rho \quad (3.42)$$

Finally, the 4x3 image-to-world transformation matrix is calculated by:

$$T_{ik} = T_k^{-1} S^T H_k \quad (3.43)$$

The experiment result is:

$$T_{ik} = \begin{bmatrix} 0.0334 & -0.0017 & -26.7584 \\ 0.01312 & -0.1815 & 24.8388 \\ -0.5363 & 0.0022 & 2408262 \\ -0.0009 & 0 & 1 \end{bmatrix}$$

With this 4x3 matrix, any given 2D laser image point can be mapped onto a 3D world point by the equation:

$$\begin{bmatrix} \bar{X} \\ \bar{Y} \\ \bar{Z} \\ \rho \end{bmatrix} = T_{ik} \begin{bmatrix} u \\ v \\ 1 \end{bmatrix} \quad (3.44)$$

Thus, the reference coordinates are $(\frac{\bar{X}}{\rho}, \frac{\bar{Y}}{\rho}, \frac{\bar{Z}}{\rho})$.

3.3.10 Results and Analysis

In order to verify the feasibility of the calibration method, the 3-D laser points corresponding to the stripe peak pixels detected in the calibration images are

reconstructed by equation 3.44. In Fig. 3.28, these points are indicated by red color and the green points are the calibration points correspondingly obtained by the method introduced in section 3.3.4 (see Fig. 3.26). Table 3.2 shows the reconstruction errors relative to the calibration points. From this table, one can conclude that based on the calibration points, the 2-D to 3-D mapping correspondence can be defined by the matrix T_{ik} .

the laser points (red) computed by Eqn. 3.44

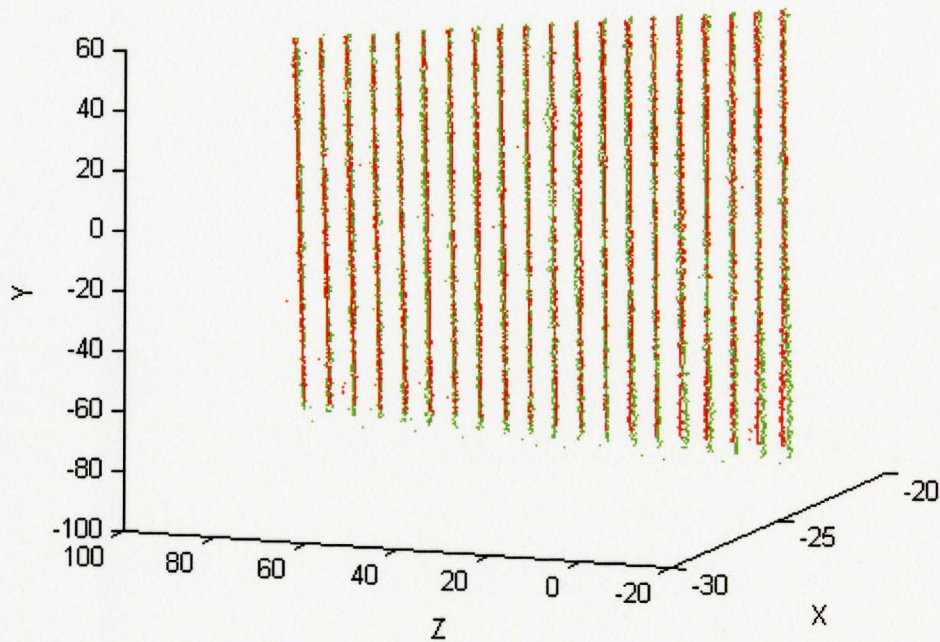


Figure 3.28: The detected laser points (in red) reconstructed by equation 3.44 (Axis scales in *mm*).

Table 3.2: Reconstruction errors relative to the calibration points

Error	X (mm)	Y(mm)	Z (mm)	deviation distance (mm)
Mean square error	0.1276	0.5028	0.3758	0.5803

However, the accuracy of this calibration method is determined by the locational accuracy of calibration points. The X , Y coordinates accuracies have been discussed in section 3.3.3 and they mainly depend on the accuracy of image processing for laser stripe segmentation and homography computation. Since the Z -coordinate of a calibration point is equal to the robot displacement with 0.1mm accuracy (see Table 3.3), this can be used as a reference to compare to the corresponding one computed by equation 3.44 so as to see how good this calibration method is. Fig.3.29 shows the comparison result, where Z values of the calibration points are from 0mm to 90mm with 5mm by each step and the maximum mean square error is 0.5998mm at zero position. From this result, it was seen that 3-D point acquisition by this calibration method is quite reliable and accurate for shape reconstruction.

In addition, a measurement example is shown in Fig. 3.30, in which the length measured by the vision system is 68.91mm and 68.10mm by a digital caliper, so an error of 1.2% has committed. Beside the innate calibration error, the measurement error is mainly caused by the optical diffusion effect, due to which some excessive pixels are counted in laser stripe detection.

Table 3.3: Determination of Z-coordinate of calibration points

steps	Z coordinate value of calibration points (mm)	Robot displacement along Z reference axe (mm)
0	0	393.36
1	5	398.386
2	10	403.359
3	15	408.358
4	20	413.360
5	25	418.362
6	30	423.354
⋮	⋮	⋮
16	80	473.333
17	85	478.328
18	90	483.332

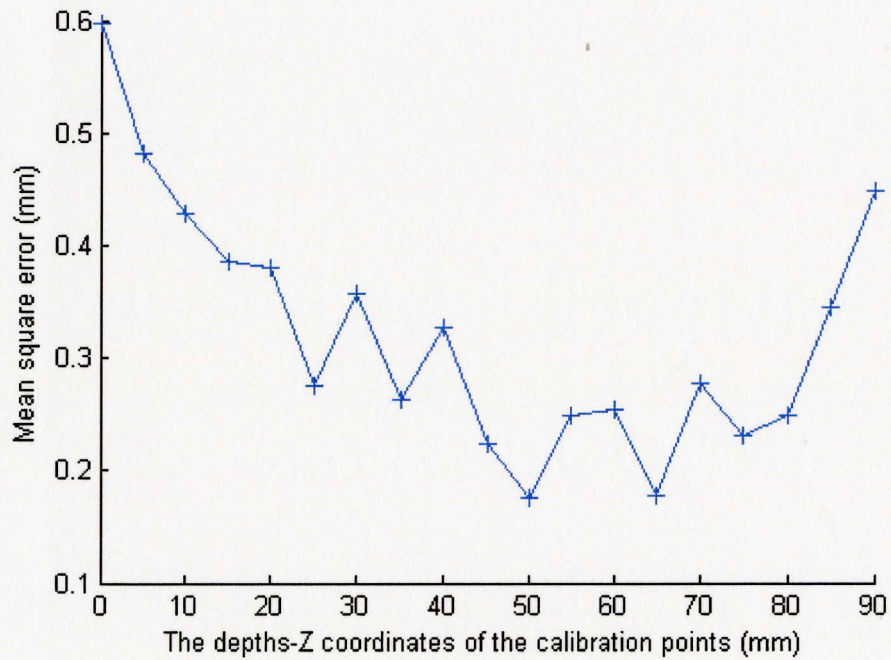


Figure 3.29: The results of depth comparison.

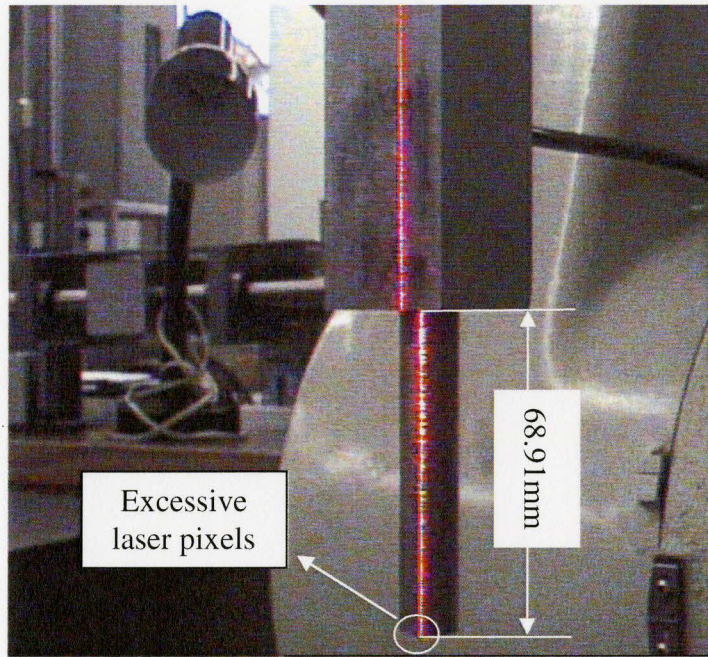


Figure 3.30: A length measured with the proposed calibration method.

3.4 360-Degrees Measurement

In following sections, a 360-degree measurement is introduced. In this measurement, a cylindrical scanning scheme is adopted to gather 3-D points from the entire surface of a workpiece. A Kawasaki six-axis robot is used to manipulate it and provide the scanning movement. A specific data structure-range image is employed to store the image coordinates of the laser stripe peaks in sub-pixel accuracy. By using this range image, noise deduction is implemented by means of local smoothness test and mean filter. Finally, a filtered point cloud of a workpiece is achieved for the cross-section reconstruction algorithm.

3.4.1 Scanning Schemes

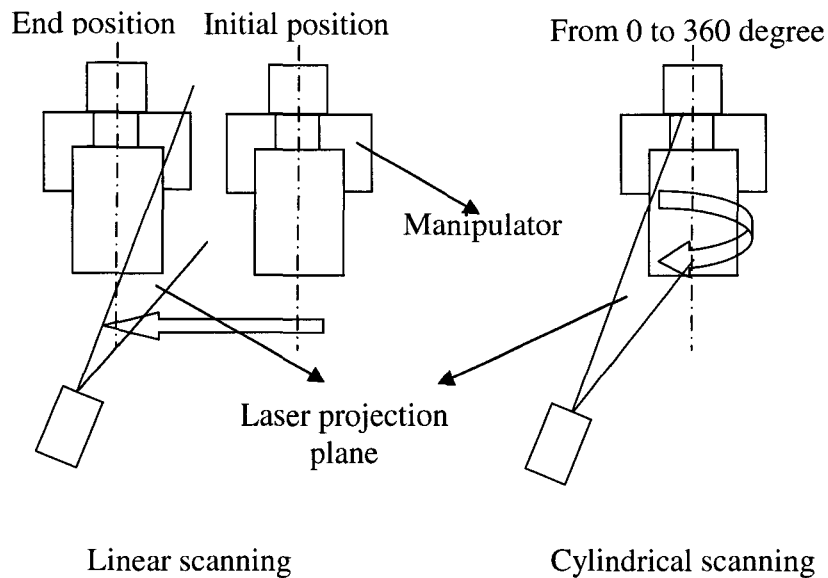


Figure 3.31: Linear and cylindrical scanning process.

Given an image of projecting the laser beam onto a workpiece, the illuminated pixels can be detected with sub-pixel accuracy and transformed into a set of 3-D points by equation 3.44. But such process only captures one view of the workpiece. In order to acquire data from the entire surface, the workpiece is swept by the vision system through the laser plane either in translational or rotational mode while the camera takes a sequence of pictures. In practice, there are two schemes applied - linear scanning and cylindrical scanning as shown in Fig. 3.31.

In these two schemes, linear scanning is commonly used by most vision systems. Though compared to cylindrical scanning, it has the advantage to avoid the occlusion problem due to which some areas of objects may not be viewed, the drawback is more scans from different views need to be made and integrated into a common coordinates system by using an iterative registration algorithm, which is a time-consuming process. Because during the integration process, the overlapped areas between consecutive views are produced and some unknown errors of movement in registration are inevitably created, the overall measurement result would be influenced by these propagated uncertainties. Therefore, in this thesis a cylindrical scanning is chosen for data acquisition.

While scanning, the workpiece measured is held and rotated by the manipulator. Its displacements and rotational angles are directly retrieved from the robot controller. Once the axis of the manipulator is determined in the reference system, the transformation matrix used for registration can be easily calculated. Using this advantage, 360-deg 3D measurement for the whole surface of the workpiece is realized.

3.4.2. Cylindrical Scanning

The program for the cylindrical scanning is described in the Fig. 3.33. The rotational movement is around the axis of the sixth joint that is placed in parallel with the Y -axis of the reference system, and both axes are aligned to be perpendicular to the ground level. The robot is commanded to rotate 360 degrees to cover the whole profile of workpiece. During rotation, the camera acquires scan images every $\Delta\phi$. At each position of the workpiece, the rotational angle ϕ_i from the initial position can be calculated by:

$$\phi_k = k\Delta\phi \quad (3.45)$$

Where k can be $1, 2, \dots, N$. N is the total number of the scan images taken around the workpiece.

In return to the initial position, all laser points of the scan lines can be considered to rotate around Y axis by $-\phi_i$. Thus, the transformation matrix of rotation is:

$$Rot(Y, -\phi_k) = \begin{bmatrix} C(-\phi_k) & 0 & S(-\phi_k) & 0 \\ 0 & 1 & 0 & 0 \\ -S(-\phi_k) & 0 & C(-\phi_k) & 0 \\ 0 & 0 & 0 & 1 \end{bmatrix} \quad (3.46)$$

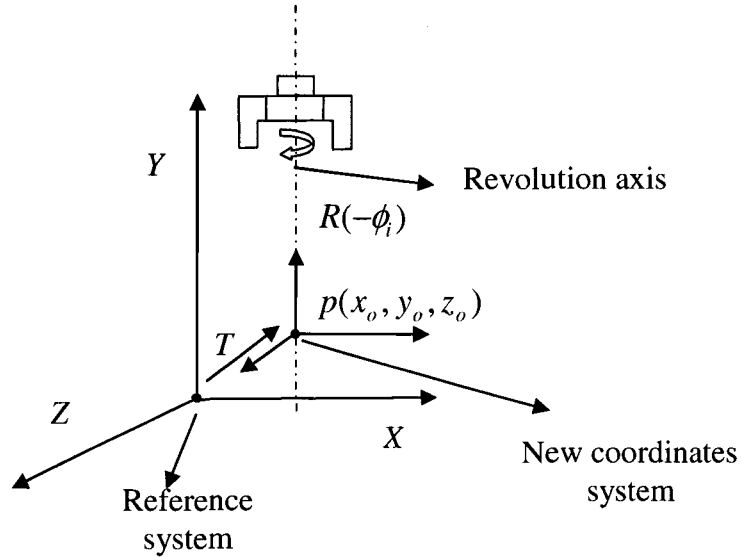


Figure 3.32: Position of the revolution axis in the reference system.

However, as shown in Fig. 3.32, the Y -axis of the reference system is not in alignment with the axis of the sixth joint but both are adjusted to be parallel to each other. There would be three components of offsets between them along X , Y , and Z axes of the reference frame. Assume that a point $p(x_o, y_o, z_o)$ lies on the revolution axis in the reference system and is considered as the origin of a new coordinates system, so the translation matrix from the reference system to the new system is given by:

$$T = \text{Trans}(-x_o, -y_o, -z_o) = \begin{bmatrix} 1 & 0 & 0 & -x_o \\ 0 & 1 & 0 & -y_o \\ 0 & 0 & 1 & -z_o \\ 0 & 0 & 0 & 1 \end{bmatrix} \quad (3.47)$$

Therefore, multiply the equations 3.46, 3.47, and the image-to-world matrix T_{ik} obtained from calibration, 3-D coordinates of a laser point in a new coordinates frame can be calculated by:

$$\begin{bmatrix} X \\ Y \\ Z \\ 1 \end{bmatrix} = Trans(-x_o, -y_o, z_o) Rot(Y, -\phi_k) T_{ik} \begin{bmatrix} u \\ v \\ 1 \end{bmatrix} / \rho \quad (3.48)$$

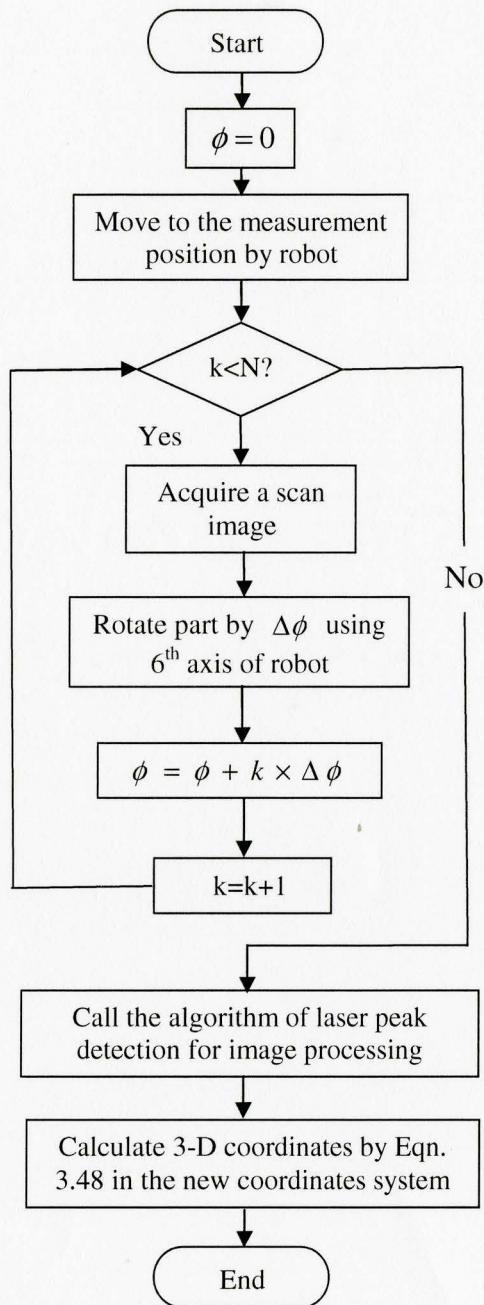


Figure 3.33: The program of cylindrical scanning vision measurement.

3.4.3 Determination of the Revolution Axis of the Manipulator in the Reference system

During cylindrical scanning, the measurement accuracy is mainly determined by the robot movement and the position of the revolution axis with respect to the reference coordinates system. Since the first factor depends on the mechanical features of the hardware and it is almost invariable in overall scanning process, precisely locating the revolution axis would be a major factor to enhance the measurement accuracy. The method to do it is given by following steps.

First, the axis of the sixth joint of the robot is aligned with the Z-axis in the base coordinates system of the robot and is perpendicular to the ground. The position of the camera is also adjusted to be on the ground level so that the image plane is parallel to the axis of the sixth joint.

Second, a fixture is designed to determine the revolution axis. As shown in Fig.3.34, it is composed of a flange and a flat plane. In the plane surface, there is a straight line drawn to be perpendicular to the flange surface and passing through the center of the flange. The flange surface is well machined and connected with the 6th joint by using four bolts. Two dowels are used to align the centerline with the revolution axis. Thus, the centerline defined by the straight line is considered as the revolution axis.

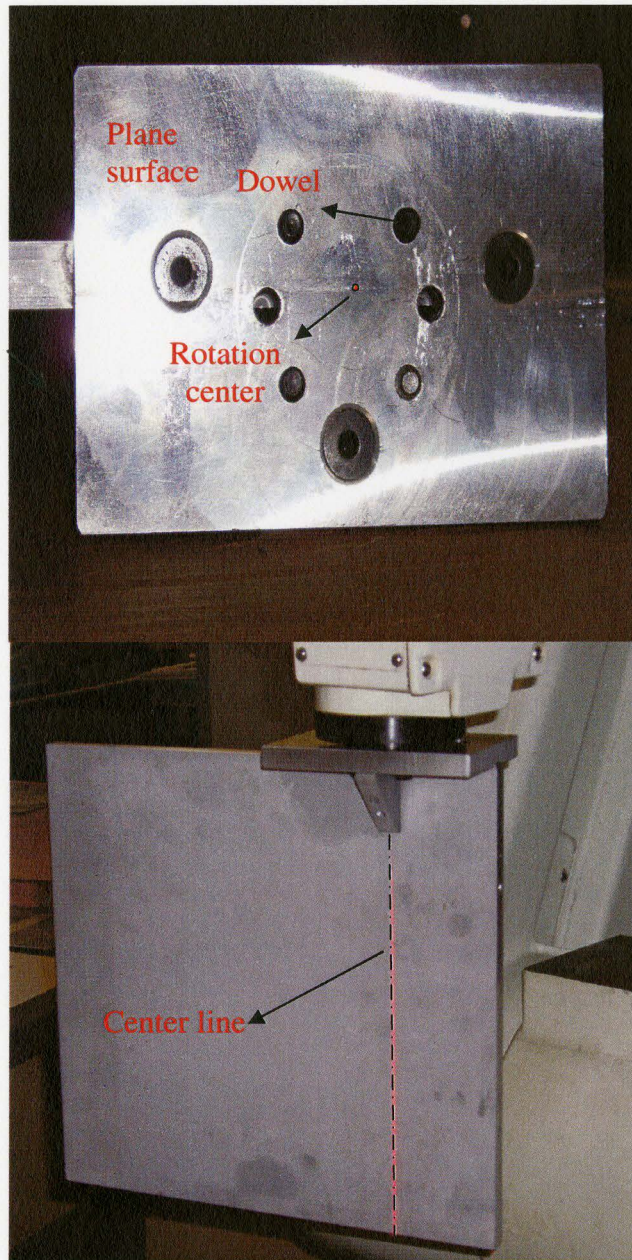


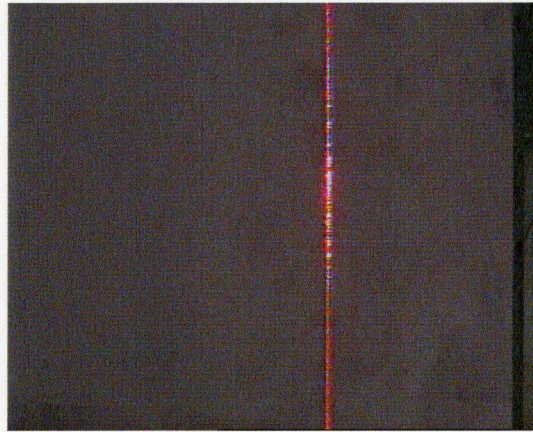
Figure 3.34: A fixture to position revolution axis.

Third, before calibrating the vision system, the laser projector is appropriately displaced and adjusted until the laser line that is projected onto the fixture is coincident with the straight line and viewed to be vertical in the image plane. Then the calibration

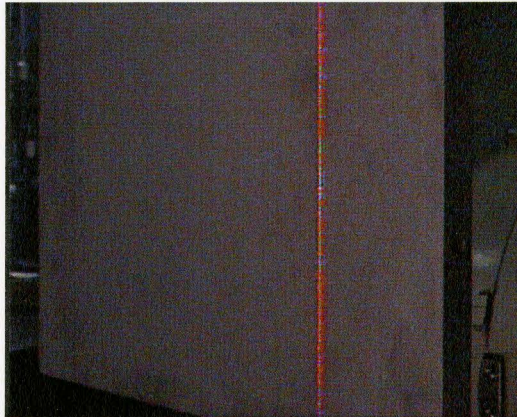
target-a checkerboard is attached to the plane surface of the fixture and the Y -axis of the reference system is adjusted to be parallel with the straight line. Therefore with such apparatus alignment, the calibration method introduced in section 3.3 is implemented.

Fourth, the image containing the fixture shot by the laser is processed to extract the illuminated pixels, with which the corresponding 3-D laser points on the revolution axis can be defined with respect to the reference coordinates system. By choosing an axis point as the origin of the new coordinates system, the translation matrix (equation 3.24) can be calculated.

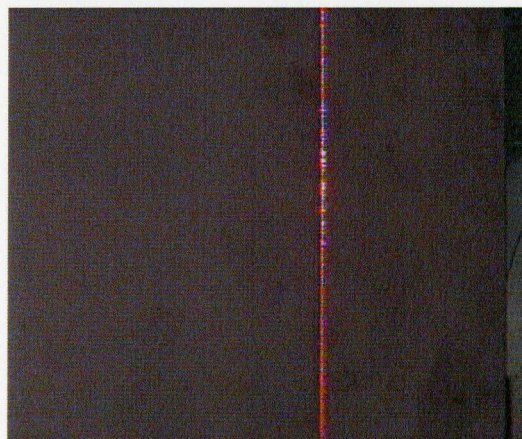
For testing this method, rotate the fixture at 0° , 30° , -30° . As viewed in Fig. 3.35, the laser line is always projected onto the straight line, which means the laser projection plane passes through the revolution axis.



0 degree



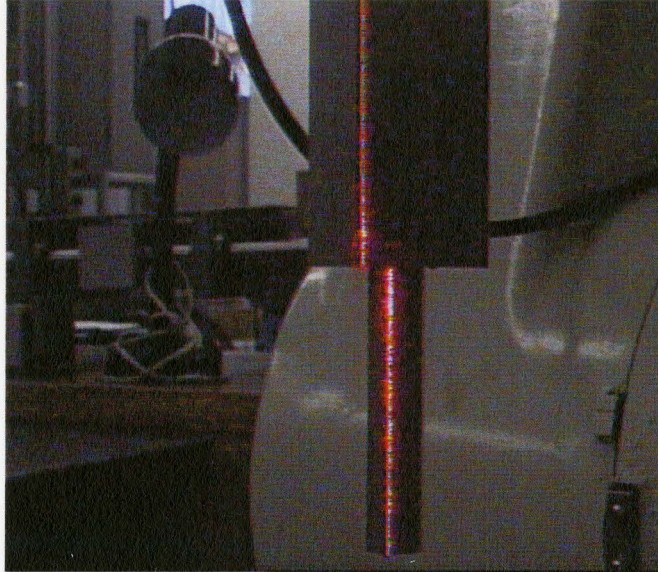
30 degree



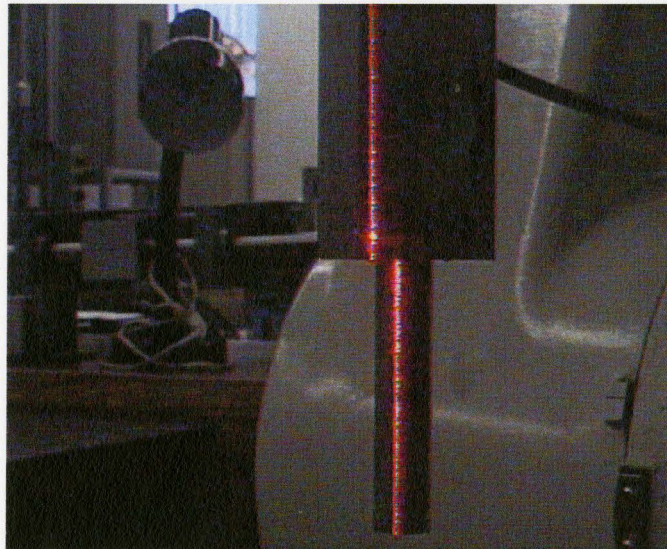
-30 degree

Figure 3.35: A laser line projected on the fixture at different angels

3.4.4 Point Cloud



0 degree



356 degree

Figure 3.36: Cylindrical scan Images of a workpiece

Fig.3.36 shows an example of cylindrical scanning. The first and last scan images record the positions of a workpiece at rotation angle 0 degree and 356 degree. The angle between two consecutive scan images is 4 degrees.

The resultant point cloud produced by this scanning is shown in Fig. 3.37, in which there are 48708 points detected. But this is a noisy collection of data and needs to be further processed by filtering. Before doing that, it is necessary to store the point cloud into an organized data structure so that the adjacencies and the geometric features of points can be easily determined.

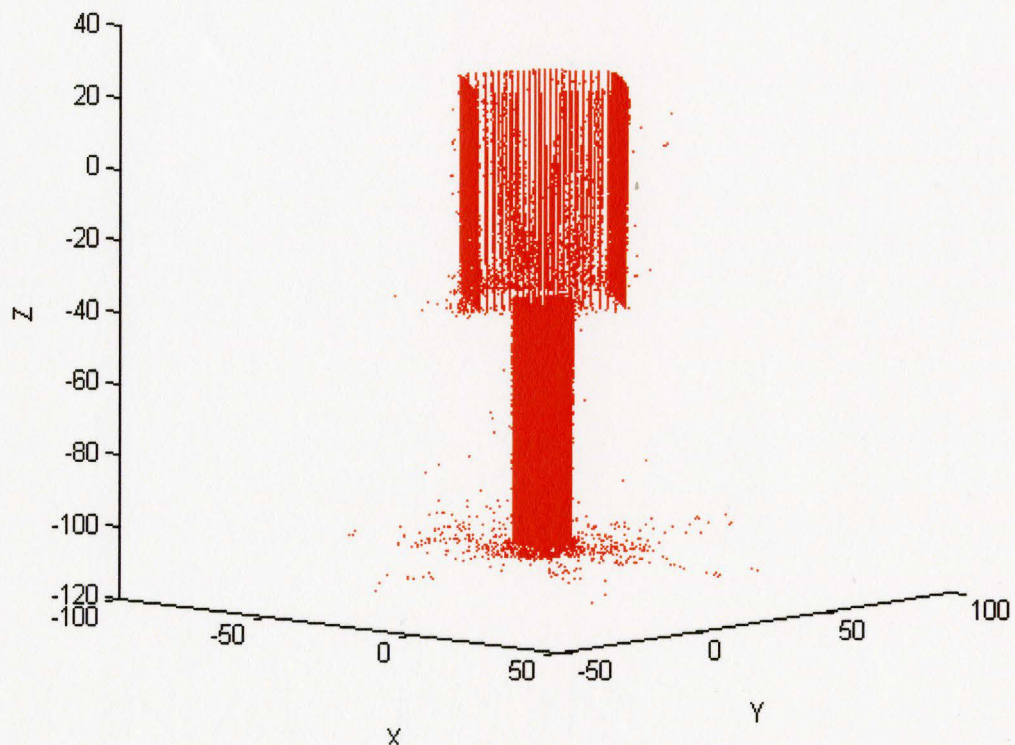
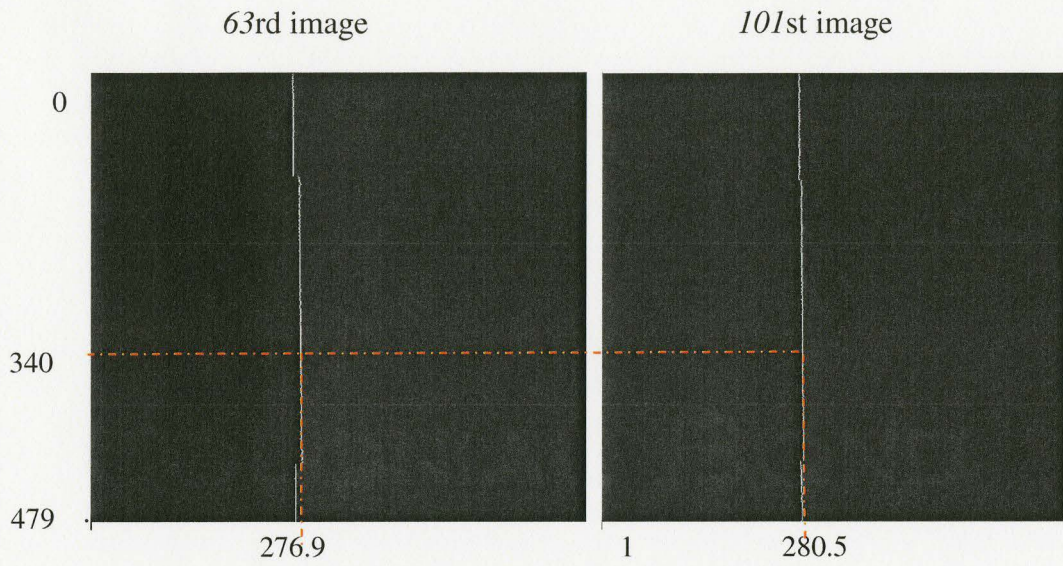


Figure 3.37: Noisy point cloud (Axis scales in *mm*)

3.4.5 Range Image

During a laser scan, a sequence of images is created by the camera, and can be stored in a more compact data structure called range image or depth image (Park and Souza, 2004). A range image may have a variety forms depending on the range sensor used for creating it (Spaidis and Besl, 1995). In this thesis, since the input points are given in an inherent order, a range image can be constructed by measuring a $m \times n$ grid depth of surface points beyond the image plane, where each grid point is defined to be a 3-D point, m is the number of the rows of camera image, and n is the total number of scanning images in sequence. Assume that the column coordinate of the laser point at the i th row in the j th image can be considered as the intensity of the pixel (i, j) in a range image. The column coordinate is computed in sub-pixel accuracy as described in section 3.2.2. In the case when no laser point is detected, the intensity is set to be -1. Fig. 3.38 depicts an example of a range image and it is visualized in Fig.3.39.



Data structure of range image

Image	63	101
Row					
⋮					
339	-1	277.1		280.3	
340	-1	276.9		280.5	
341	-1	277.2		280.7	
⋮		⋮		⋮	

Figure 3.38: A data structure to store the laser points in sub-pixel accuracy.

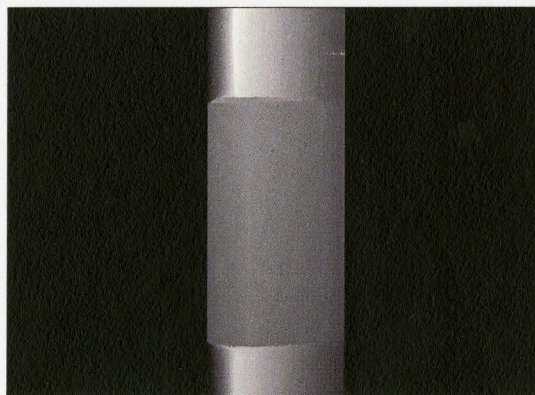


Figure 3.39: An example of range image.

From the definition above, in a range image made by cylindrical scans, the row i is related to the rotation angle around the Y -axis of the reference system, j the Y -axis and intensity r is related to the depth Z -axis. Since a range image is maintained in a grid, some collection of neighboring points at any given grid point can be directly produced.

3.4.6 Noise Elimination

In a vision system, data taken from any given position only shows what is visible from that location. It is possible that the point may be deviated or missed due to the noise. In this section, two methods are introduced to eliminate the noise: local smoothness test and mean filter.

1. Local smoothness test

The most significant noise that exists in data acquisition with a scanner is multi-peak problem, in which more than one laser peak pixels occur in a row of image as shown in Fig. 3.40. The principle of choosing the peak with strongest intensity would fail in this case to detect the illuminated point in the primary reflection of the laser. There are two main reasons to produce this noise. One is surface specularly resulting in inter-reflections (shown in Fig. 3.41) among surface points, which is made worse by a shiny surface. Another is saturation mainly caused by strong lighting conditions, due to which some pixels with the highest intensity would be randomly distributed across the object surface.

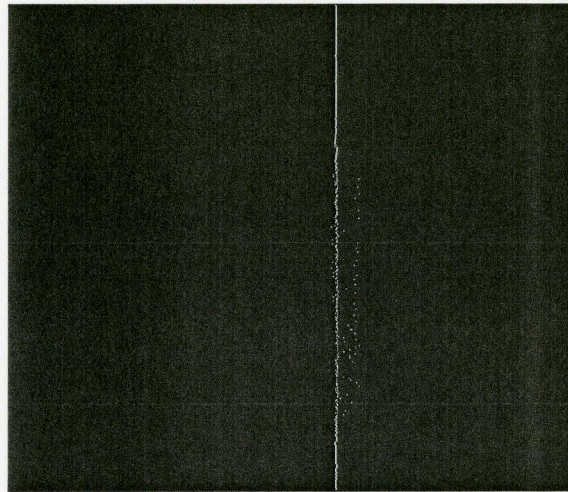


Figure 3.40: Multi-peaks problem.

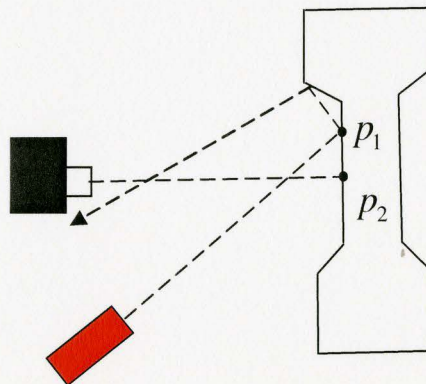


Figure 3.41: Inter-reflection phenomenon. p_1 is truly illuminated and p_2 is a false point.

In experiments, an aluminum bar is measured with the slit scanner. When the laser is projected onto the bar, some of the laser light may scatter off the bar surface to illuminate another part of the bar as shown in Fig. 3.42. As a result, some false points may be generated and sensed by the camera, the presence of which would make it difficult to localize a data point that corresponds to a truly illuminated point (Park and Kak, 2004).

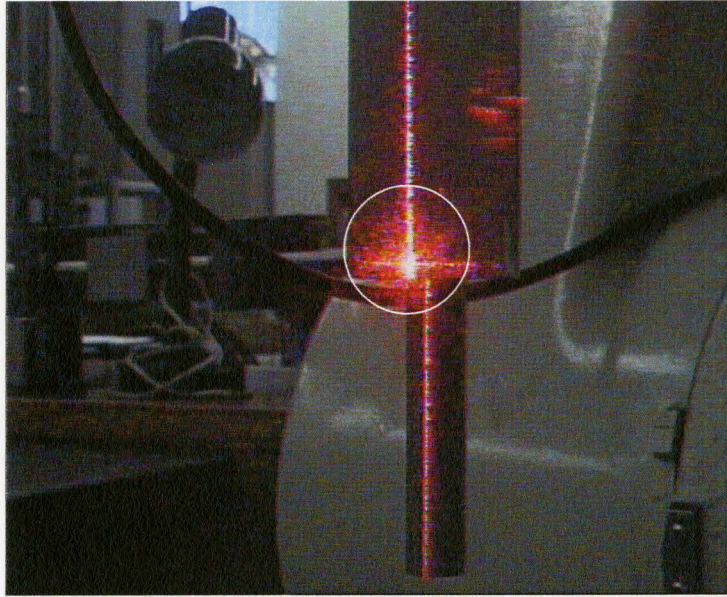


Figure 3.42: A bar illuminated by the laser

Park and Kak proposed a local smoothness test to deal with this problem (2004). It is based on a legitimate assumption that given a true measured surface point p_i , a local planar patch can be reasonably fitted around this point within a small window. If there is not a suitable planar patch found, this measurement is doubted and should be eliminated. With this criterion, two constraints are used to determine the planarity. The first constraint is the number of valid points in the fitting window. If the number $m(p_i)$ is greater than a threshold τ_m :

$$m(p_i) > \tau_m \quad (3.49)$$

this point is accepted, otherwise discarded. The valid data points are those that have distances to the interest point are not larger than a threshold d_{\max} . Because the vertical (referred to as the distance between two neighboring pixels) and horizontal sampling resolutions of the range image are significantly different, in programming, two thresholds

are selected for this distance judgment. One is $d_{p \max}$ related to the camera resolution for the points in a same scanning line, and another is $d_{s \max}$ related to the sampling resolution for the points in two scanning lines.

The second constraint is the fitting error \mathcal{E} which is determined by the average Euclidean distance from the window points to the best fitting plane. Suppose there are n valid points in a fitting window for p_i , including p_i itself. With the least squares method introduced in section 3.3.5, the plane is fitted, so that the normal vector can be obtained. Then the dot product of the vector of each point to the center of mass x_c of fitting points with normal vector is simply considered as the Euclidean distance between a point and the fitting plane. Thus, the fitting error is calculated with:

$$\mathcal{E}(p_i) = \frac{1}{n} \sum_{e=1}^n [x(p_e) - x_c] \bullet n(p_i) \quad (3.50)$$

In experiments, the small window is defined as 3x3 (3 is the number of scan images and the row of image pixels) around an interest point in a range image. Through tests, a good performance can be achieved by the threshold values chosen as follows:

Table 3.4: The threshold values for local smooth test

Threshold	τ_m	$d_{p \max}$	$d_{s \max}$	\mathcal{E}
Values	4	0.8mm	1.0mm	0.01mm

Figures 3.43 and 3.44 shows the experimental results based on the noisy point cloud in Fig.3.37.

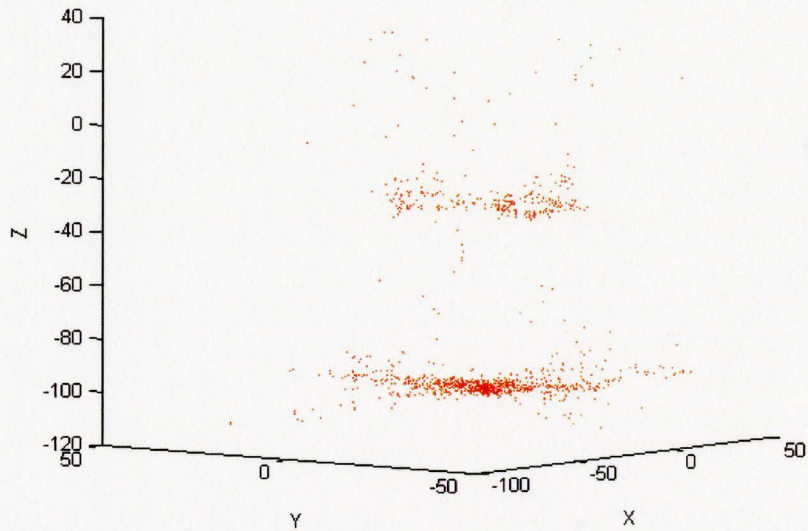


Figure 3.43: Noise points detected through filtering (Axis scales in *mm*).

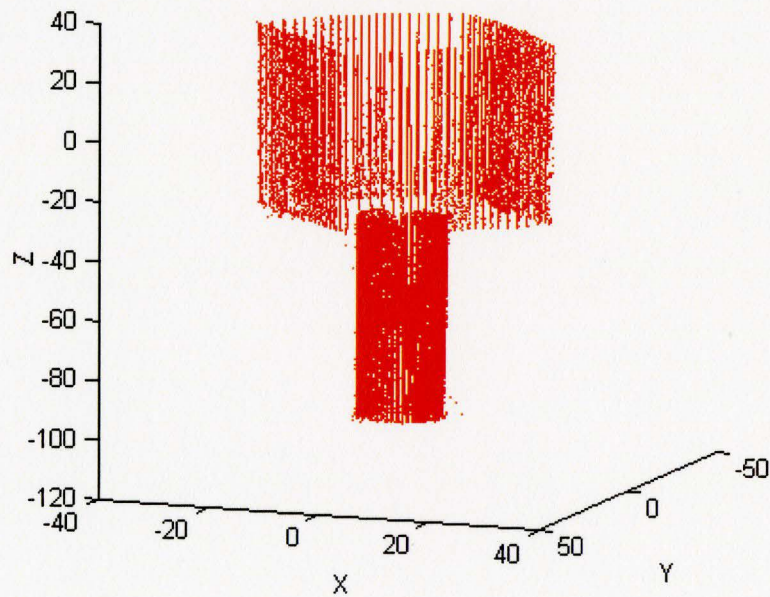


Figure 3.44: The resultant point cloud after local smoothness test (Axis scales in *mm*).

2. Mean filtering

The points cloud acquired by a scanner is a loosely defined topology. Adjacency between points is determined by some adjacency defined by the scanner like sampling sequence and neighboring pixels at the same scanning line. But due to limited sampling resolution, some points may be “missing” – no return to the sensor occurs where adjacent points are expected. Some erroneous facets like spike might be generated in surface reconstruction. Therefore, the mean filter is employed to fill the gap and smooth the range image (Weinstein, 2006).

The algorithm for this filter takes advantage of the grid structures in a range image. Assume that the intensity values around an interest point should be smoothly distributed.

Based on this assumption, a weighted average of intensities of a point’s neighbors is taken to find a new intensity. Thus, the algorithm goes by:

- For each point p in a range image, find the set of neighboring pixels by using a 3×5 window.
- Find the median intensity c_m in this set.

$$c_m = \frac{1}{n} \sum_{i=1}^n c_i, \quad (3.51)$$

Where:

n is the number of adjacent pixels in a 3×5 window

c_i is the intensity value of the i^{th} pixel

- The intensity of the interest point is calculated by:

$$p_{\text{intensity}} = \frac{\sum_{i=1}^k w_i c_i}{\sum_i w_i} \quad (3.52)$$

Where:

$$w_i = e^{-d_i^2/\sigma^2}, \text{ the weight for each point}$$

c_i = the intensity of the i^{th} point in the 3×5 window

$$d_i = |c_i - c_m|$$

σ = mean difference of intensity values from c_m

The reduced points in local smoothing test also can be made up in the same algorithm. The result of this filtering is shown in Fig.3.45.

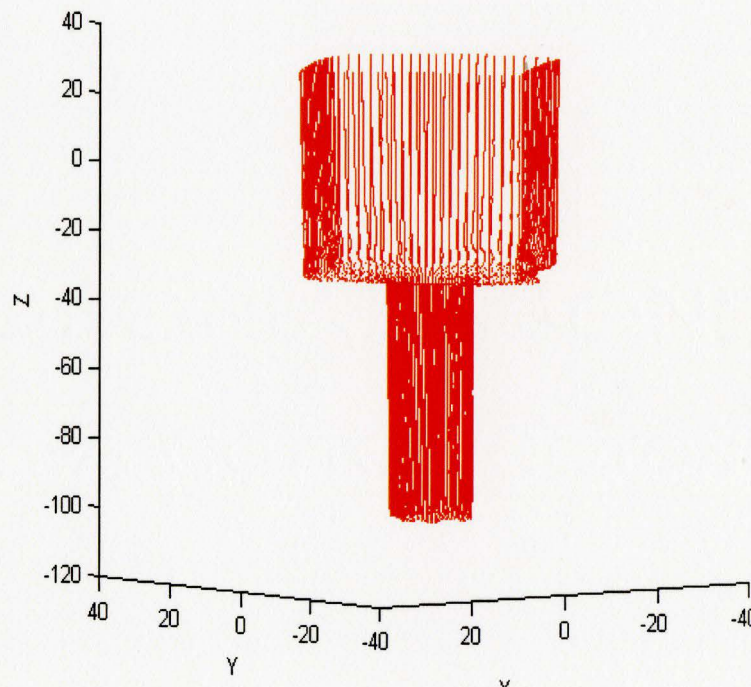


Figure 3.45: The result of median filter (Axis scales in mm).

3.5 Geometry Measurement in Intelligent Open Die Forging System

During the forging process, the shape of a workpiece is not regular and so it is more difficult to perform the geometry measurement. In order to make automatic measurement, the shape reconstruction of a workpiece must meet the demand of shape error detection in the intelligent open-die forging system. In this section, a cross section reconstruction algorithm is introduced. The reasons for using it will be discussed in following.

3.5.1 Function of the 3-D Vision System in Intelligent Forging System

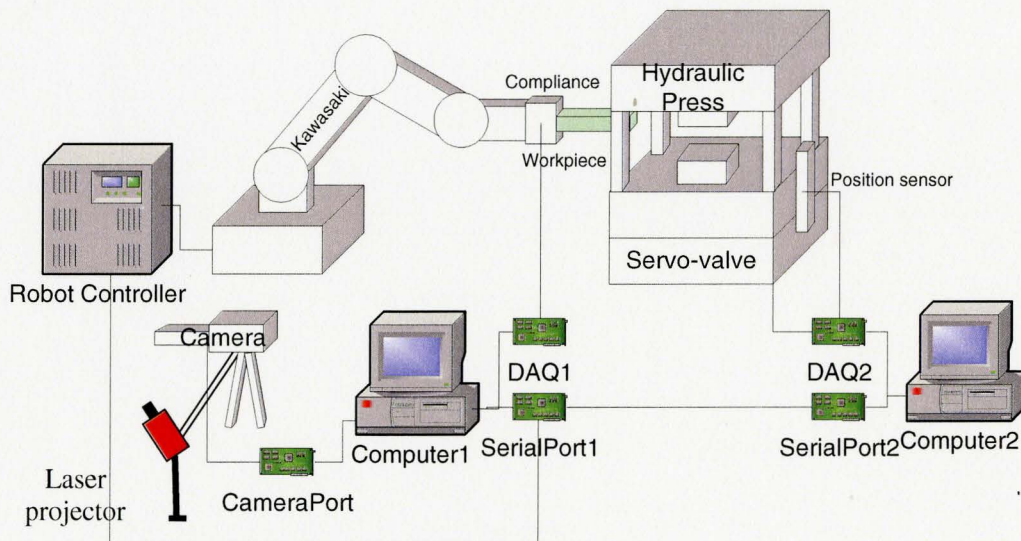


Figure 3.46: An intelligent open-die forging system (revised from Ma's system).

In this thesis, the 3D vision system exists in an intelligent open die forging system as

shown in Fig. 3.46. The function of the forging system is to automatically form a workpiece into a desired shape. A forging strategy is similar to that of a blacksmith. The implementation of it can be done in the following steps:

1. Measurement. The feature geometries of a workpiece like cross sections and length are measured by a vision system.
2. Comparing. Based on the results from measurement, the shape errors between current shape and target shape are detected. Also the spread coefficient is calculated to predicate the shape in next forging pass.
3. Moving and rotating. If the maximum shape error is less than the tolerance, the forging process can be stopped, otherwise it continues. The workpiece is moved and rotated where the maximum error occurs for the next step of forging.
4. Forging. A hydraulic press is commanded to forge the workpiece with a certain load determined by the forging behavior

Induced from this forging strategy, the core of the control program in intelligent forging system is the feedback of the shape error. The 3D vision system serves as a measurement unit to detect it. However, the difficulty in this detection is how to determine the shape of a forged part and what criterion is adopted to make the forging strategy.

3.5.2 Shape Error Detection

Generally, in forging, to determine if the geometry is correct, the following dimensions are considered (Goldstein and Wright, 1985):

1. Cross-sectional area. This area is considered as a measure of the amount of material present at cross-sectional positions.
2. Thickness and width. These are considered jointly as they determine the proportioning (i.e. thickness to width ratio) of the open-die forging.
3. Length. The bottom of the workpiece is used as a reference for all other vertical dimensions.

In the above criteria, Items 1-2 are concerned with cross-sectional features and are measured by performing cross-sectional reconstructions. Item 3 relates to vertical dimensions measured by analyzing profiles from many cross-sections along the center line of a workpiece.

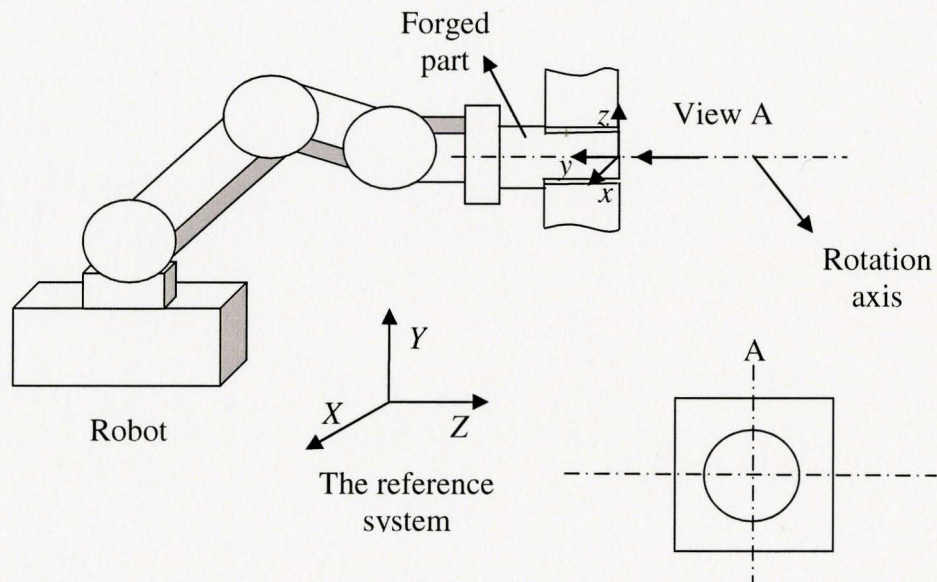


Figure 3.47: The process of forging a workpiece by a robot.

Within the context of an intelligent forging, due to the fact that the forged part is held and manipulated by the robot in press, the process of shaping it can be considered as the

squeezing operations along the revolution axis of the manipulator as shown in Fig. 3.47. If this revolution axis is regarded as the center line of a workpiece, the cross sections along it would form the entire surface of a workpiece. By comparing the current cross section with the desired one at each length, the shape error can be easily achieved by the program.

On the other hand, when the maximum error of a cross-section is detected at a length, the manipulator will move the part to the corresponding position in the press and rotate it so that the line linking the measured point with the maximum error and a rotation axis point is perpendicular to the horizontal contact surface of the dies. As a result, the vision system should provide the length and rotation angle where the maximum error occurs.

3.5.3 Application in the Cylindrical Scanning Vision System

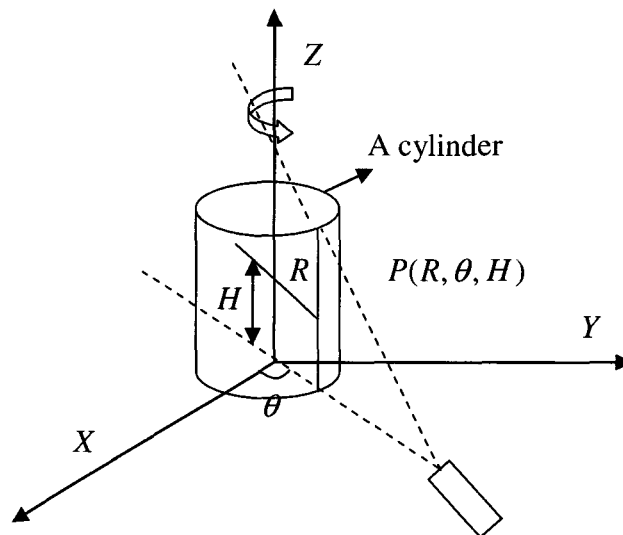


Figure 3.48: A cylindrical scanning model.

During cylindrical scanning, the laser projection plane always passes through the revolution axis of the manipulator. Assume the workpiece held by the manipulator is regarded stationary while the laser projector is considered as rotating 360 degree around the workpiece as shown in Fig. 3.48. At a rotation angle, a laser line can be created by the intersection of the laser plane with the workpiece surface. If a point on the laser line is measured by the vision system, its position can be determined with a cylindrical coordinate (R, ϑ, H) , in that θ corresponds to a rotation angle of the laser plane, H is the height of a cross-section calculated from its Y Cartesian coordinates in the new coordinates system (see Fig.3.32), and R is the distance from this point to the center of the cross-section assumed to be passed by the rotation axis, and is computed by the equation:

$$R = \sqrt{X^2 + Z^2} \quad (3.53)$$

Where X, Z are Cartesian coordinates of this point in the new coordinates system.

A desired corresponding cross-section can be obtained from the intersection of the target shape and a plane with a height H . Therefore, the measurement error between a desired and measured point in the same rotation angle θ is:

$$error = r - R \quad (3.54)$$

Here, r is the distance from this desired point to the axis point.

According to the discussions above, in this thesis, the algorithm for shape reconstruction is to detect the cross-section at any place along the revolution axis and define the position of the measured points as a cylindrical coordinate (R, ϑ, H) .

3.5.4 Reconstruction Algorithm of a Cross-Section of Workpiece at a Height

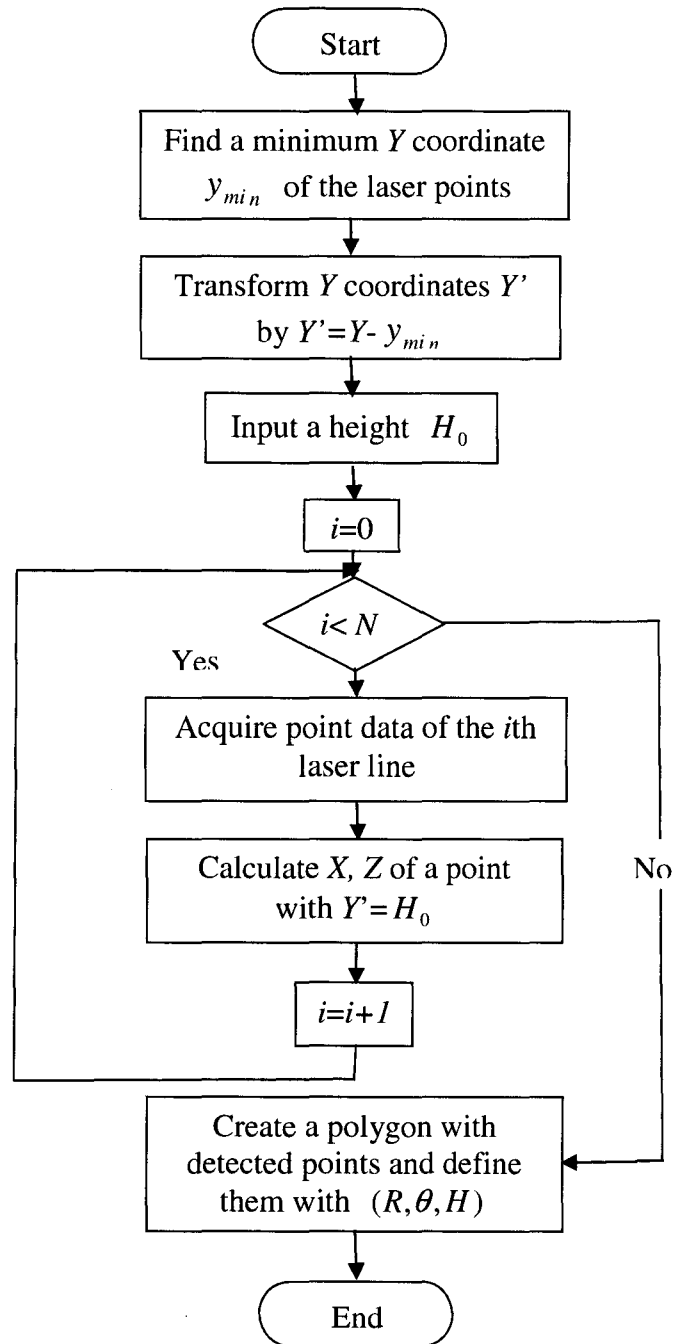


Figure 3.49: Flow chart of the cross-section reconstruction.

Fig. 3.49 shows the flow chart of the shape reconstruction algorithm. The difficulty in shape reconstruction arises from the fact that the three-dimensional changes in the configuration of workpiece. Within a Cartesian coordinates system, the position of a forged part is determined by the position of the griper. In the intelligent forging system, due to material deformation, a robot compliance device is designed to accommodate the elongation and sideway spread of the part, so that the damage to the griper can be avoided. As a result, the position of the part is always changed with the position of the griper. Thus, the shape reconstruction cannot be made based on a fixed coordinates system.

In this thesis, assume the centerline of a workpiece is always along the revolution axis of 6th joint which is identical to the Y -axis in the new coordinates system, and the workpiece moves along the axis during forging process. Based on this assumption, after the measured points are acquired, the reconstruction algorithm first tracks a point with the minimum Y coordinate y_{\min} . Then move the origin of the new coordinates system to this lowest surface point along Y -axis. Thus, the Y coordinates of all points are changed by:

$$Y' = Y - y_{\min} \quad (3.55)$$

Where Y' is used to denote the measured height H of a workpiece, the bottom surface of the workpiece is considered as the reference at $H=0$.

At a rotational angle, a laser line is created. It is composed of a group of dense points. Two adjacent measured points can be connected by a 3-D short line. Thus, any point between them can be interpolated by a 3-D line equation, given by:

$$\frac{X - X_0}{a} = \frac{Y - Y_0}{b} = \frac{Z - Z_0}{c} \quad (3.56)$$

Therefore, when $Y' = H_0$ of this point, its X, Z coordinates can be calculated by:

$$\begin{cases} X' = k_1(Y' - Y_1) + X_1 \\ Z' = k_2(Y' - Y_1) + Z_1 \end{cases}$$

And,

$$k_1 = \frac{Y_1' - Y_2'}{X_1 - X_2}, \quad k_2 = \frac{Y_1' - Y_2'}{Z_1 - Z_2} \quad (3.57)$$

Here (Y_1, X_1, Z_1) and (X_2, Y_2, Z_2) are the coordinates of two adjacent measured points, (X', Y', Z') is one of points between these two points.

As a result, when all the points with the same height H_0 are obtained from a point cloud around a workpiece, they can be linked into a closed-loop polygon, which would form a cross-section of the part at H_0 . In this way, many cross sections along Y -axis can be reconstructed from the measurement data. In each cross section, a point P is defined as:

$$P = (R_0, H_0, \theta_0) \quad (3.58)$$

Where, R_0 is computer by the equation 3.31, θ_0 is the rotation angle of a laser plane.

3.6 The 3-D Measurement Software

All the programs discussed in this chapter integrate to form 3-D measurement software. The sub-programs in it include: serial communication monitoring for robot control, laser peak detection for image processing, cylindrical scanning for 3-D data acquisition, noise elimination for data filtering and cross-section reconstruction for geometry measurement. The flow chart of the software is displayed in Fig. 3.50 and its performance will be discussed in next chapter.

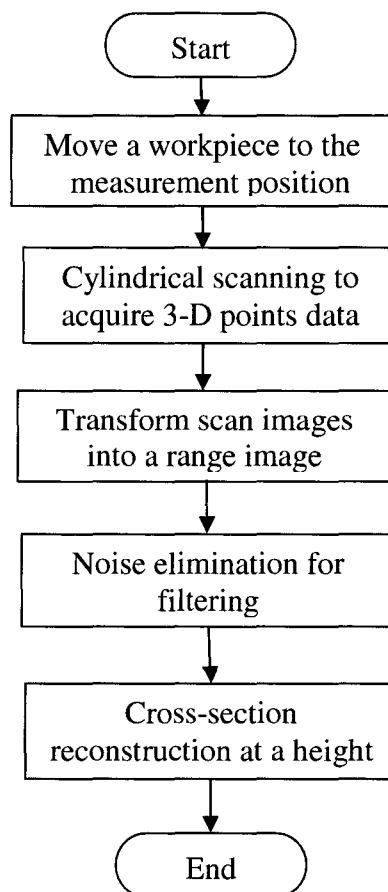


Figure 3.50: The flow chart of 3-D measurement software.

Chapter 4

Experimental Results and Analysis

This chapter reports on the results obtained during the test of the 3-D vision system explained in chapter 3. Since the validation of 3-D point generation for obtaining point correspondences created by the calibration algorithm has been reported in chapter 3, only the performance of cross-section reconstruction is described here. However, the overall accuracy of modeling is not discussed in this thesis.

4.1 Experimental Results

The experiment consists in scanning a well known object with simple geometric features. A cylinder which is part of a workpiece is chosen for this object with diameter $\phi = 15.07mm$ and *height*=68.10mm, measured with a digital caliper with 0.01mm accuracy. The scan images of this workpiece have already been introduced in section 3.4.4. Before the experiment, the bottom surface of the cylinder is aligned to be at ground level, so that its center line can be approximately parallel to the 6th joint axis and the little inclination between them is ignored in this experiment.

After noise elimination, the resultant point cloud has been shown in Fig.3.45. Using the cross-section reconstruction algorithm, the 3-D shape of the workpiece is explicitly

displayed in Fig. 4.1. With this representation, each cross-section can be fitted into a circle with the least squares method. Fig. 4.2 shows the fitted circles along the height from 5 to 68mm. Therefore, the reconstructed diameters with a certain fitting error are compared to the actual diameter for error analysis. The results are given in Fig 4.3-4.5.

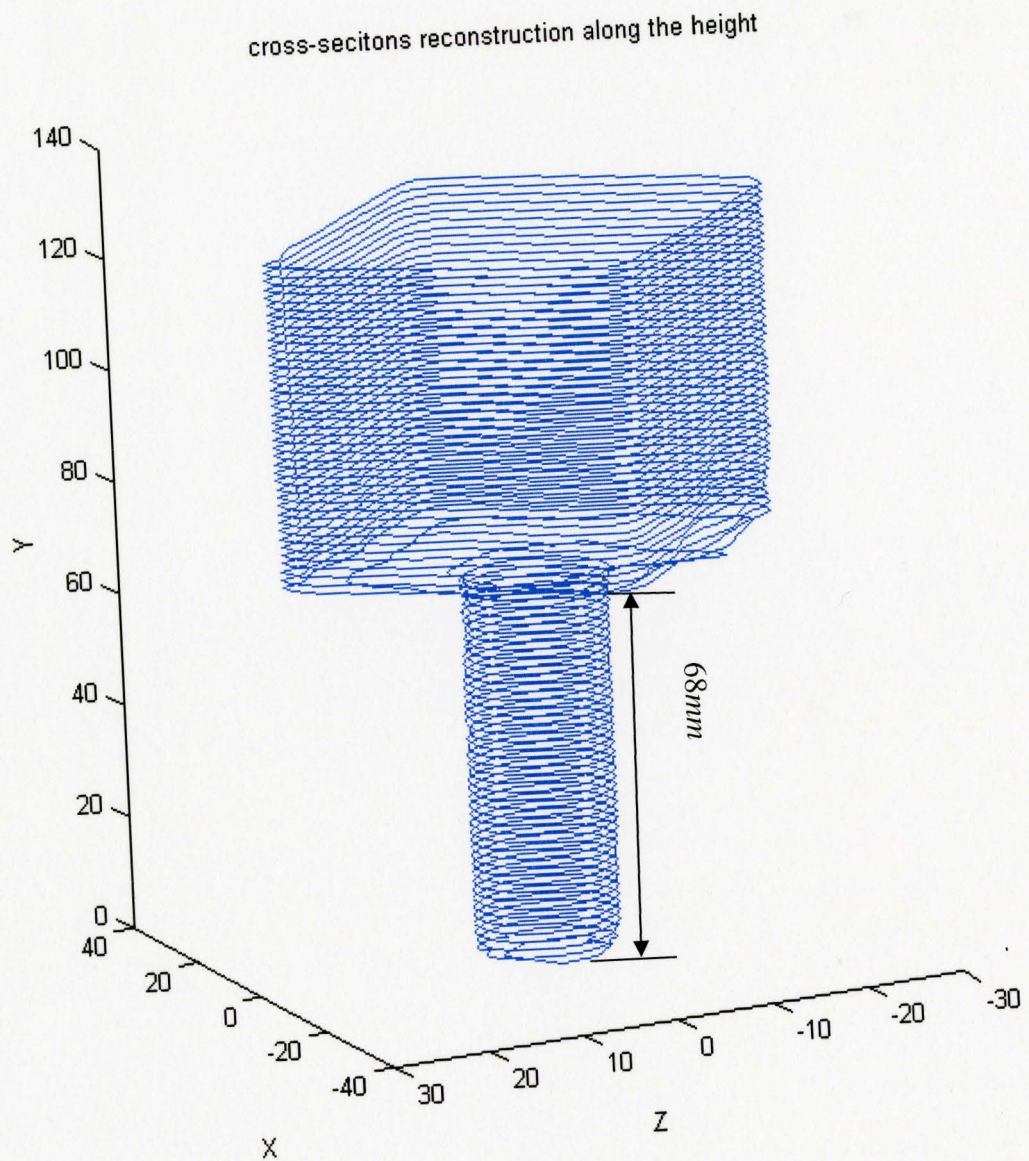


Figure 4.1: 3-D shape by cross-section representation (Axis scales in *mm*).
Where, the height between two adjacent cross-sections is 1.5mm.

A cylinder $d=15.07\text{mm}$

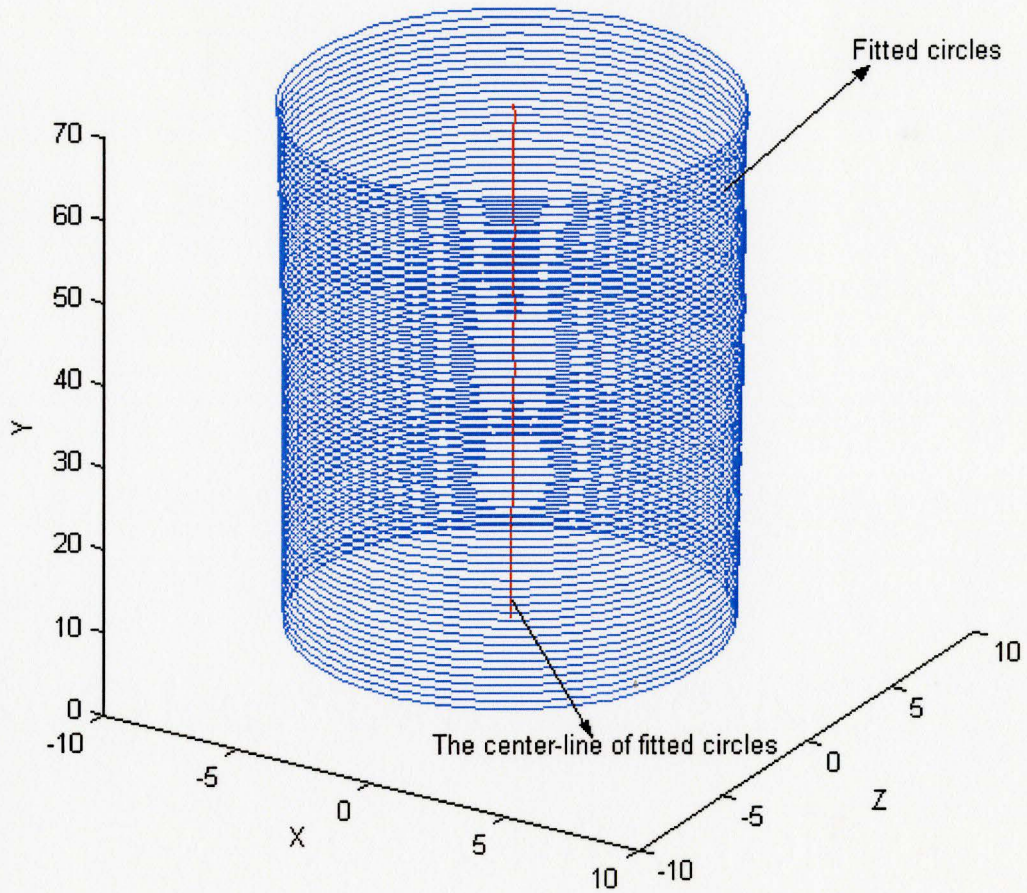


Figure 4.2: Reconstruction of a cylinder by cross-section representation, along the height from 5mm to 68mm (Axis scales in *mm*).

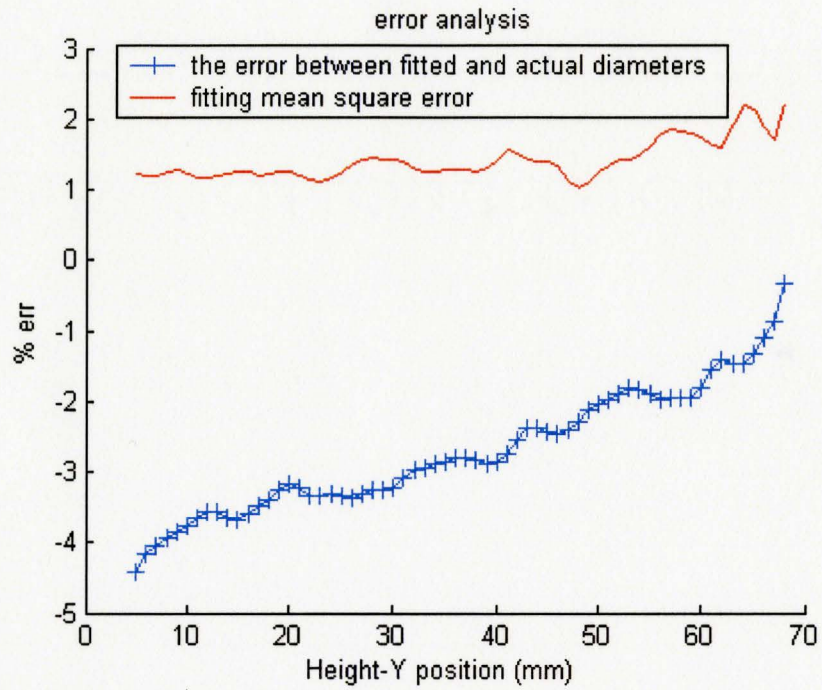


Figure 4.3: The errors of circle fitting and reconstruction diameter along the height

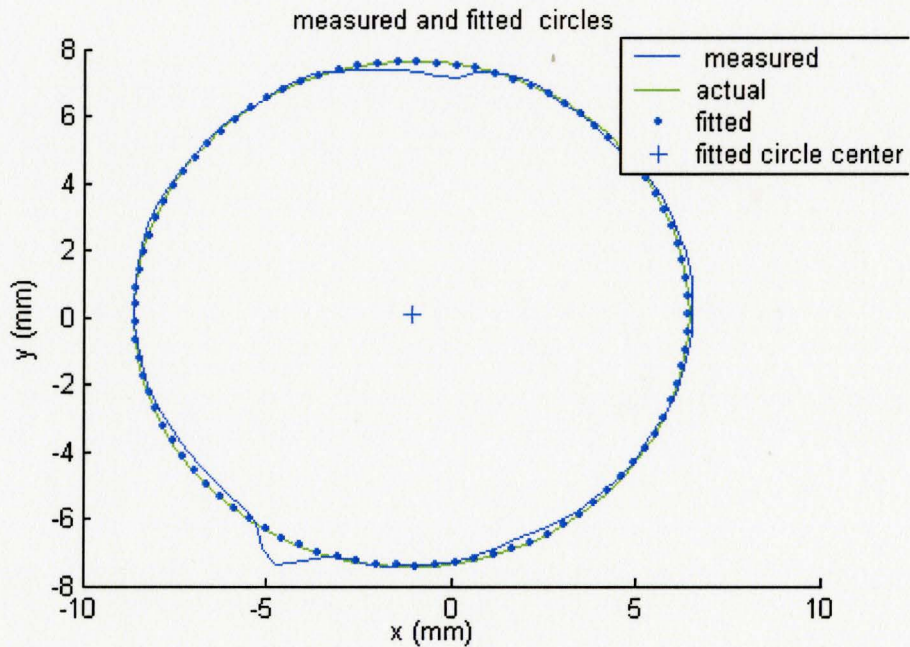


Figure 4.4: A fitted circle at height=68mm. The fitting mean square error is 0.32mm, and the error between reconstructed and actual diameters is 0.7%.

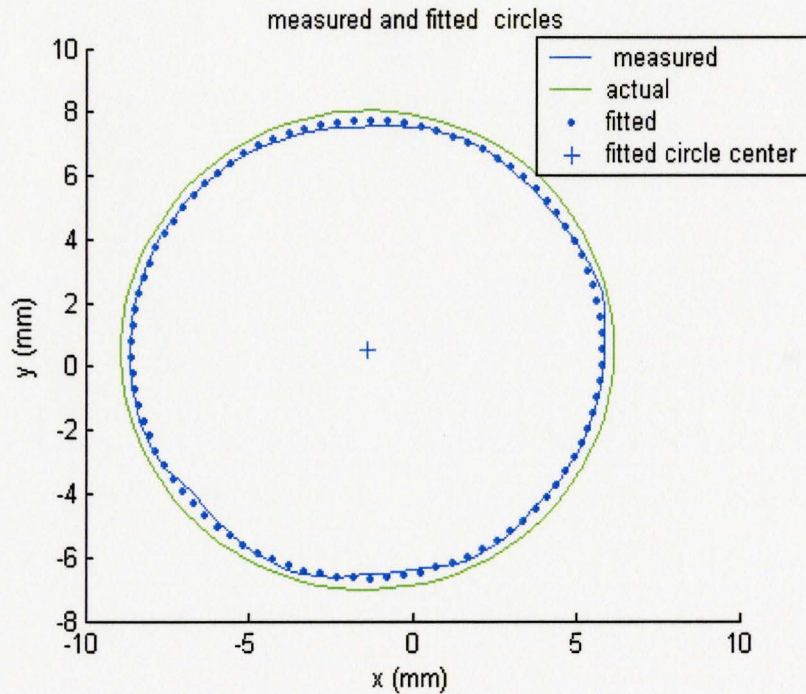


Figure 4.5: A fitted circle at height=5mm. The fitting mean square error is 0.18mm, and the error between reconstructed and actual diameters is 4.4%.

4.2 Analysis

As can be seen in Fig.4.3, along the height from 5mm to 68mm, the captured cross-section of the cylinder is quite close to the round shape with a fitting error less than 2.1%. But the fitted circle is a little off the actual size. The largest deviation with 4.4% error was found near the underside of the cylinder (see Fig.4.5). The reason is the misalignment of the Y -axis with the revolution axis of the 6th joint. While calibrating the robot, because the parallelism of these two axes was not adjusted accurate enough, there exists a slight rotation transformation between them other than translation. As a result, since the origin of the new coordinate system is fixed above the cylinder in the experiments (see Fig.3.45), the reconstruction diameter errors were expected to have a

definite trend to approach zero with the increasing height.

On the other hand, it was also found some cross-sections assume fuzzy shapes as shown in Fig.4.6-4.7. These failures are mainly caused by two reasons. One is noise reduction. This mostly occurs at the bottom surface where much noise created by the optical diffusion effect is eliminated through the local smoothness test (see Fig.3.30 and Fig.3.43). Another is the effect of mean filter due to that the discontinuous edge between round and square shapes of the workpiece is smoothed.

Despite the shortcomings above, the performance of the vision system is quite satisfactory through the evaluation, since it is built with the simple and low-cost components. To this end, a 3-D shape of an actual forged part is reconstructed as shown in Fig.4.8. Its free-formed shape has been well captured, and will be useful for shape error detection in the forging cell.

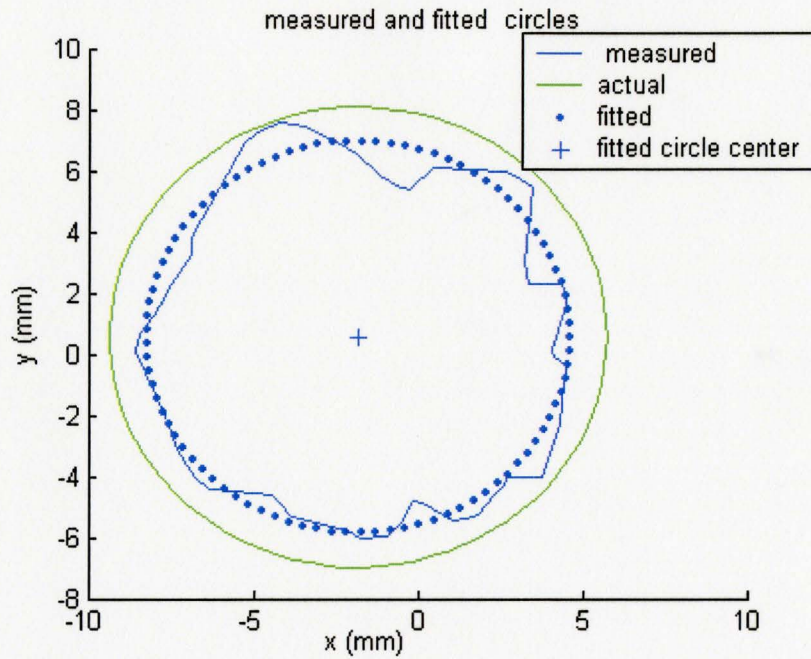


Figure 4.6: A fitted circle at height=1mm. The fitting mean square error is 1.12mm, and the error between reconstructed and actual diameters is 15%.

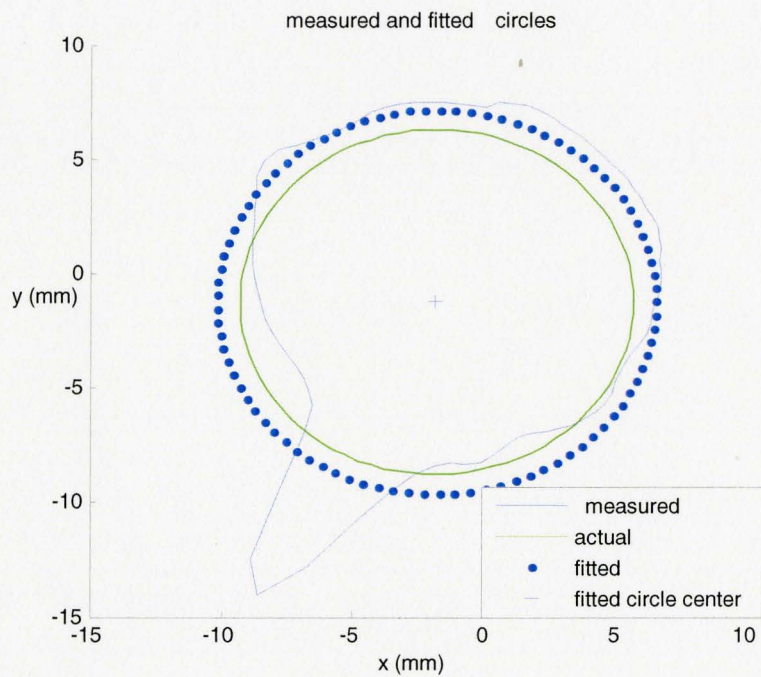


Figure 4.7: A fitted circle at height=69mm. The fitting mean square error is 2.72mm, and the error between reconstructed and actual diameters is 11%.

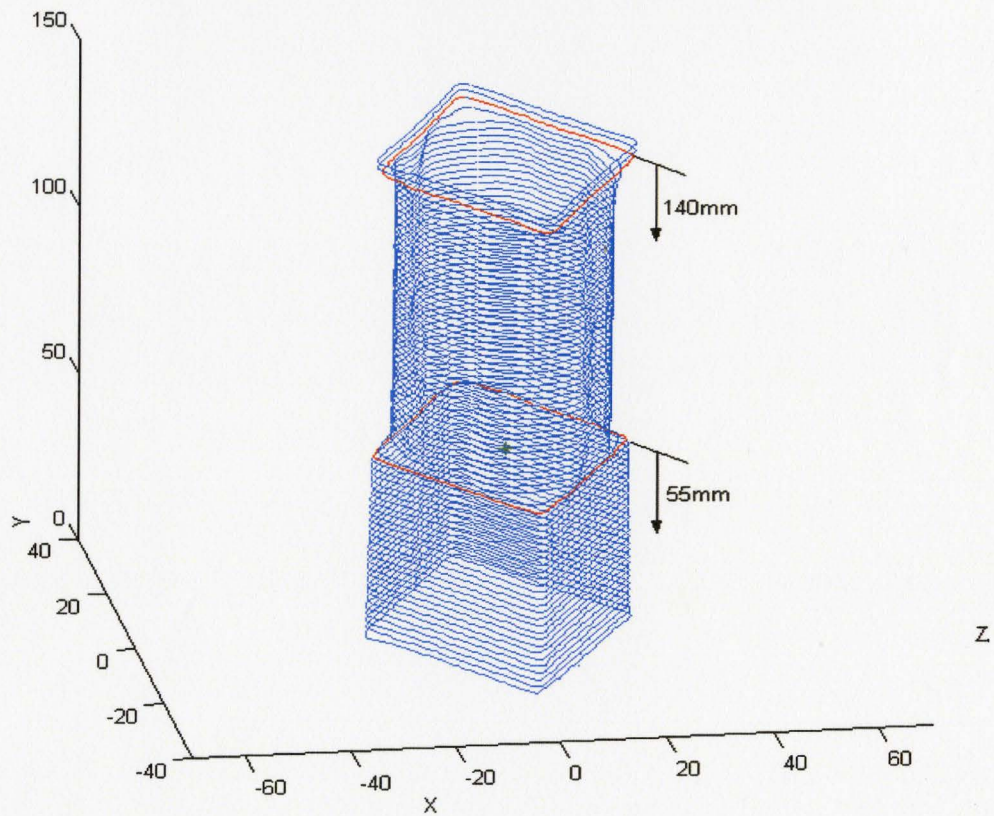
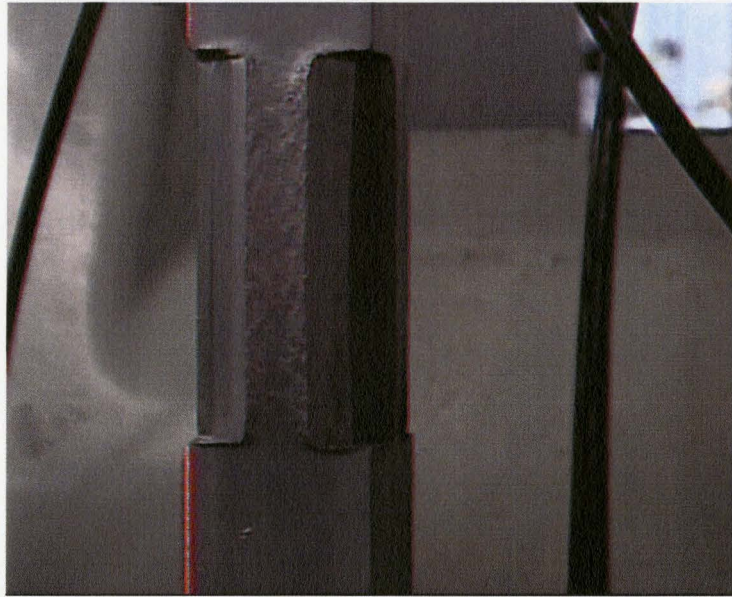


Figure 4.8: A forged part reconstructed by 3-D vision system (Axis scales in *mm*).

Chapter 5

Conclusions and Recommendations

5.1 Conclusions

In this thesis, a 3-D vision system is built up for real time measurement. The function of this system is to acquire 3-D point data from entire surface of a workpiece and reconstruct its cross-section at any place along the height, so that its shape is fully recovered and then will be used to detect shape error for adaptive control of intelligent open-die forging system. This vision system was successfully tested on a workpiece consisting of a cylinder shape. Although some fuzzy cross-sections occur when too much noise and sharp edges exist in the reconstruction process, the overall shape achieved is worthy to be trusted.

Accomplishments are summarized as:

1. The technique of linear structured light is applied for 3-D data acquisition. Compared to other methods, this technique has the benefits of low-cost, more accuracy and simple hardware components.
2. A laser stripe segmentation algorithm is proposed. This algorithm uses the methods of red color tracking and thresholds in RGB channels to subtract the

background around a laser stripe, so that the stripe can be successfully extracted in an open environment without any optical filter.

3. Gaussian estimator is applied to determine the stripe peak positions in sub-pixel accuracy. This estimator fits a Gaussian profile to three adjacent intensities around the brightest stripe pixel. The position at zero crossing of the first derivative in this profile is considered as the stripe peak. Compared to COM3 estimator, it is more reliable especially when a shiny or rough surface is scanned.
4. An easy and practical calibration method is developed. The simplicity of this method exists in its implementation only with a laser-printed chessboard and a fast projective algorithm for determining 2-D to 3-D mapping correspondence. Unlike classical methods based on closed-form models, the camera intrinsic and extrinsic parameters and structured parameters need not to be calibrated. This reduces the cost and time of measurements and improves the real-time ability of laser scanning. Experiments conducted for this method verify that it is robust and capable of producing good accuracy for shape measurement tasks.
5. A cylindrical scanning scheme is applied for gathering data about the 3-D shape of parts. 360-degree scan images of a workpiece can be captured by this scheme and then merged into a common coordinates system with robot transformation matrix. In order to realize this integration, a special fixture is designed to determine the position of the 6th joint axis in the reference system. The great advantage is the overlap problem which is inevitable in linear scanning scheme is easily resolved.

6. Local smoothness test and mean filter are employed to reduce the measurement noise. As a result, the large false measurements generated by multi-peaks are eliminated and a set of smooth point data is achieved for next shape reconstruction.
7. A cross-section reconstruction algorithm is proposed to recover the 3-D shape of a forge part. Concluded from the test results on a cylinder shape, this algorithm is proved to have the ability of providing 3-D shape for shape error detection.

5.2 Recommendations for Future Work

1. Methods of reducing measurement noise could be studied to eliminate or reduce the amount of mean filtering, so that the overall modeling accuracy is less affected by it. This may be resolved by using an extra camera to detect the correct laser projection. When the image points captured by two cameras have the same 3-D position, the measurement is considered to be true, otherwise to be false.
2. The calibration of the revolution axis with respect to the reference coordinates system could be modified for best reconstruction accuracy. The mathematical alignment should be made between the 6th joint axis and the *Y*-axis of the reference system so as to achieve the rotation matrix other than translation.
3. Forging strategy for forming complicated shapes like convex and concave could be achieved based on the 3-D vision measurement system set up in this thesis.
4. Spread coefficient needs to be calculated according to the geometries of part, so that the forming behavior in next forging pass can be predicted in advance.

References

- Akaskal, B., F. H. Osman, and A. N. Bramly. *Upper-bound analysis for the automation of open-die forging*. Journal of Materials Processing Technology 71, pp.215-223, 1997.
- Bottema, O. and Roth, B. *Theoretical Kinematics*. North-Holland: Amsterdam, 1979.
- C.H. Chen and A.C. Kak. *Modeling and calibration of a structured light scanner for 3-D robot vision*. In Proceedings of the IEEE conference on robotics and automation, pp. 807-815, 1987.
- D.Garcia, J.J. Orteu, and M. Devy. *3D deformation measurement using stereo-correlation applied to experimental mechanics*. The 10th FIG International Symposium on Deformation Measurements, Session 2: New techniques in monitoring surveys 2, pp.50-60, 2001.
- D. Q. Huynh, R. A. Owens, and P. E. Hartmann. *Calibrating a Structured Light Stripe System: A Novel Approach*. International Journal of Computer Vision 33(1), pp.73-86, 1999.
- E. Siemer, P. Neischwitz, R. Kopp. *Quality optimized process control of open die forging*. Stahl Eisen 21, pp.383–387, April 1986.
- E. Trucco, R.B. Fisher, A.W. Fitzgibbon, and D.K Naidu. *Calibration, data consistency and model acquisition with laser stripers*. Int. J. Computer Integrated manufacturing, Vol 11, No. 4, pp. 293-310, 1998.
- F. Blais. *Review of 20 years of range sensor development*. Journal of Electronic Imaging 13(1), pp. 231–240, 2004.
- F. Blais, M. Rioux, and J.-A. Beraldin. *Practical considerations for a design of a high precision 3-D laser scanner system*. Proc. SPIE 959, pp. 225–246, 1988.
- Fei Zhang and Bin Kong. *Calibration of Linear Structured Light System by Planar Checkerboard*. Proceedings of International Conference on Information Acquisition, pp. 344-346, 2004.
- F. Liu, F. Duan, and S. Ye. *A new method for the calibration of line structured light sensor using zigzag target*. Meas. Tech. 7, pp.3–6, 1999.
- Frank Chen, Gordon M. Brown, Mumin Song. *Overview of three-dimensional shape measurement using optical methods*. Optical Engineering 39(1), pp.10–22, January 2000.

- Goldstein, M. and P.K Wright. *A fast algorithm for high accuracy gauging using computer vision*. Robotics & Computer-Integrated Manufacturing 2, pp.105-113, 1985.
- Jenson, J.E. *Forging Industrial Handbook*. Forging Industry Association, 1966.
- Johny Park and Avinash C. Kak. *Multi-peak Range Imaging for Accurate 3D Reconstruction of specular Objects*. The 6th Asian Conference on Computer Vision, 2004
- Johnny Park and Guilherme N. Desouza. *3D Modeling of Real-World Objects Using Range and Intensity Images*. Innovations in Machine Intelligence and Robot Perception, 2004.
- Kawasaki Robotics (USA), Inc. *A/AD Controller Operations and Programming Manual*. 28059 Center Oaks Court: Kawasaki Robotics (USA), Inc, Jan 1995.
- Kawasaki Robotics (USA), Inc. *AS Language Manual*. 28059 Center Oaks Court: Kawasaki Robotics (USA), Inc, October 2001.
- K. H. Strobl, W. Sepp, E. Wahl, T. Bodenrniiller, M. Suppa, J. E Seara, and G. Hirzinger, 2004. *The DLR Multi-sensory Hand-Guided Device: The Laser Stripe Profiler*. Proceedings of IEEE International Conference on Robotics & Automation, New Orleans, LA , pp. 1927-1932, April 2004.
- Li Ma. *Development of An Intelligent Forging Center (thesis)*. McMaster University, 2004.
- Muhammad Ali, Javed Rabbani Shah and Masood Ahmed. *3D Reconstruction and Model Acquisition of Objects in Real World Scenes using Stereo Imagery*. Proceedings IEEE INMIC, pp.32-37, 2003.
- Nye, T. J., A. M. Elbadan, and G. M. Bone. *Real-time process characterization of open die forging for adaptive control*. Transactions of ASME 123, pp.511-516, 2001.
- Open Computer Vision Library (OpenCV). Intel, <http://sourceforge.net/projects/opencvlibrary>, 2006.
- P. J. Besl and N. D. McKay. *A method for registration of 3-D shapes*. IEEE Transactions on Pattern Analysis and Machine Intelligence, 14(2) , pp.239–256, 1992.
- R.B. Fisher and D.K. Naidu. *A comparison of algorithms for sub-pixel peak detection*. In P. Mowforth (ed.) Proceedings of the British Machine Vision Conference, Glasgow (BMVA Press), pp. 217-225, 1991.
- R. Klette, K. Schluns, A. Koschan. *Computer Vision- Three-Dimensional Data from Images*. Springer- Verlag Singapore Pte. Ltd, 1998.
- R. Y. Tsai. *A versatile camera calibration technique for high-accuracy 3D machine vision metrology using off-shelf TV cameras and lenses*. IEEE Trans, Robotics and Automation, vol. 3, pp. 323-344, 1987.

- Sergey Weinstein. *3-D Stereoscopic Reconstruction using Structured Light*. Computer Science of Boston College, http://cs.bc.edu/research/bachelors_theses/2006, pp14, 2006.
- Shaw C. Feng and Theodore H. Hopp. *A Review of Current Geometric Tolerancing Theories and Inspection Data Analysis Algorithms*. National Institute of Standards and Technology, NISTIR 4509, pp.6-9, February 1991.
- Skarbek, W., and Koschan, A. *Color image segmentation– a survey*. Tech. rep., Institute for Technical Informatics, Technical University of Berlin, October 1994.
- Slawo. W and Ed Jernigan. *Color edge detection in RGB using jointly Euclidean distance and vector angle*. Vision Interface '99, Trois-Rivières, Canada, 19-21, pp.9-11, May 1999.
- S-W. Kwon et al. *Fitting range data to primitives for rapid local 3D modeling using sparse range point clouds*. Automation in Construction 13, pp.67-81, 2004.
- Tomlinson, A., and Stringer, J. D. *Spread and Elongation in Flat Tool Forging*. J. Iron Steel Inst., London, 193, pp. 157-162, 1959.
- Zhengyou Zhang. *A Flexible New Technique for Camera Calibration*. Microsoft Research, 1999.
- Zhenzhong Wei, Guangjun Zhang and Yuan Xu. *Calibration approach for structured-light-stripe vision sensor based on the invariance of double cross-ratio*. Opt. Eng. 42(10), pp.2956–2966, October 2003.
- Zongyi Wang, Hongwei Li, Dianpu Li and Weiling Zhao. *A Direct Calibration Method for Structured Light*. Proceedings of the IEEE International Conference on Mechatronics & Automation Niagara Falls, Canada, pp 1283-1287, July 2005.
- Wistreich, J. G., and Shutt, A. *Theoretical Analysis of Bloom and Billet Forging*. J. Iron Steel Inst., London, 193, pp. 163–176, October 1959.
- V. Carbone, M. Carocci, E. Savio², G. Sansoni and L. De Chiffre. *Combination of a Vision System and a Coordinate Measuring Machine for the Reverse Engineering of Freeform Surfaces*. The International Journal of Advance Manufacturing Technology 17, pp. 263-271, 2001.